Karlsruhe Institute of Technology

Characterization Measurements of the KATRIN Focal-Plane Detector System

Master thesis
of

Agnes Seher

at the Institut for Experimental Nuclear Physics

Reviewer:	Prof. Dr. Guido Drexlin
Second Reviewer:	Prof. Dr. Wim de Boer
Advisor:	Dr. Fabian Harms

09. November 2015 – 08. November 2016

Karlsruhe Institute of Technology

Messungen zur Charakterisierung des KATRIN Fokalebenen Detektor Systems

Masterarbeit
von

Agnes Seher

am Institut für Experimentelle Kernphysik

Referent:	Prof. Dr. Guido Drexlin
Korreferent:	Prof. Dr. Wim de Boer
Betreuender Mitarbeiter:	Dr. Fabian Harms

09. November 2015 – 08. November 2016

Erklärung zur Selbstständigkeit

Ich versichere, dass ich diese Arbeit selbstständig verfasst habe und keine anderen als die angegebenen Quellen und Hilfsmittel benutzt habe, die wörtlich oder inhaltlich übernommenen Stellen als solche kenntlich gemacht und die Satzung des KIT zur Sicherung guter wissenschaftlicher Praxis in der gültigen Fassung vom 17.05.2010 beachtet habe.

Karlsruhe, den 07.11.2016, ______________________________

Agnes Seher

Als Ansichtsexemplar genehmigt von

Karlsruhe, den 07.11.2016, ______________________________

Prof. Dr. Guido Drexlin

Contents

1. Introduction

With the postulation of neutrinos in 1930 by W. Pauli and their experimental discovery in 1956 by Reines and Cowan the problem with momentum and energy conservation in the β-decay was solved. However, 14 years later the neutrino turned out yet again as mysterious particle when first experiments started to observe solar neutrinos. These experiments were based on a technique using radiochemicals and measured a flux of the electron neutrinos which differed from the predictions of the established standard solar model. Eventually, this was solved by the SNO experiment in 2002 which was the first of its kind that was sensitive to all neutrino flavors, and revealed the ability of neutrinos to change their flavor. These so-called neutrino flavor oscillations directly imply a non-vanishing rest mass of at least two neutrino flavors indicating physics beyond the standard model of particle physics. Chapter 2 gives a detailed overview of the experimental discovery of neutrinos and the theoretical description of the flavor oscillations.

The KArlsruhe TRItium Neutrino (KATRIN) experiment aims to determine the effective mass of the electron anti-neutrino. For this purpose, the energy spectrum of electrons emitted in tritium β-decay is precisely analyzed close to its endpoint $E_0 = 18.6\,\mathrm{keV}$. To achieve this goal, KATRIN makes use of a high luminosity windowless gaseous tritium source from where the β-electrons are guided along magnetic field lines adiabatically towards a combination of two electrostatic spectrometers based on the MAC-E filter principle. The latter act as high-pass filter such that only those with sufficient kinetic energy are able to pass their retarding potential and are counted by a focal-plane detector (FPD) system. With a sensitivity of $m_{\bar{\nu}_e} < 200\,{}^{\mathrm{meV}}/_{\mathrm{c}^2}$ (90% C.L.) KATRIN surpasses the sensitivity of its predecessor experiments by one order of magnitude. The different subsystems of the KATRIN experimental beamline are described in chapter 3.

The main focus of the thesis in hand is the FPD system which counts the β-electrons with a high detection efficiency. The FPD is based on a silicon PIN-diode wafer with 148 individually read-out pixels. Two superconducting solenoids provide a guiding magnetic field for the β-electrons coming from the spectrometer. Inside the system a post-acceleration electrode (PAE), allows to re-accelerate the β-electrons in order to boost their kinetic energy to regions of lower intrinsic detector background rate. A complex readout chain allows to monitor the signals in real time and further remotely operate all devices (e.g. valves, vacuum gauges, etc.). The FPD with all its subsystems is described in chapter 4.

While designed to operate at up to $+30\,\mathrm{kV}$ the PAE as currently installed in the FPD system experiences HV breakdowns at voltages $>+10\,\mathrm{kV}$. In order to improve the performance of this key system of the FPD several experiments were carried out in the context of the thesis in hand. These test were conducted with a separate test stand setup by the KATRIN collaboration partners at the University of Washington (UW) and are described in detail in chapter 5.

Initially the FPD system was developed and assembled at UW before it was shipped to the KATRIN experimental site at the Karlsruhe Institute of Technology (KIT) in 2011. Since then the system was commissioned, characterized, and operated in joint operation with the KATRIN main spectrometer in several extensive (SDS) measurement campaigns. However, even with the FPD system close to fully functioning, there is still room for improvement: During a maintenance break between two SDS campaigns, a spare wafer was installed to the system in order to characterize its performance. The results of these test measurements and a comparison to other wafer is given in chapter 6 of this thesis.

2. Neutrino Physics

The physics Nobel Prize of 2015 was awarded to T. Kajita and A. B. McDonald for the experimental observation of neutrino oscillations. This has drawn more attention to neutrino physics and the physics beyond the standard model. In this chapter a short historical overview featuring the discovery and postulation of the neutrino in the standard model of particle physics is given in section 2.1. Observations and theory concerning neutrino oscillations are described in section 2.2, followed by experimental approaches to determine the neutrino mass in section 2.3.

2.1 Neutrinos in the Standard Model - A Historical Overview

At the end of the 19th century radioactive decay was first observed. Soon three types of radiation were known: α-, β- and γ-radiation. While observing these decays it was found out for the energy spectra of α- and γ-radiation to be discrete. Though seeming like a two-body-problem Chadwick measured a continuous energy spectrum for β-decay in 1914 [1]. This violation of energy and momentum conservation did not correspond to the physical knowledge which was gained so far. To resolve this W. Pauli suggested a new particle which is additionally emitted during β-decay and electrically neutral with spin $1/2$ [2]. Instead of a two-body decay one would now observe a three-body decay which explains the continuous spectrum perfectly:

$$^{A}_{Z}\mathrm{X} \quad \rightarrow \quad ^{A}_{Z+1}\mathrm{X}' + \mathrm{e}^- + \bar{\nu}_\mathrm{e} \quad . \tag{2.1}$$

Further W. Pauli expected the mass of this particle he named “neutron” to be less than 1% of the proton mass.
Two years later Chadwick discovered during his experiments a neutral particle in 1932 [3] which was too heavy to be the one emitted out of the β-decay. It was the “neutron” as it is known today. Motivated by the previous work of W. Pauli and Chadwick, E. Fermi published his theory of the β-decay as a point-like weak interaction consisting of four fermions in 1934 [4]:

$$\mathrm{n} \rightarrow \mathrm{p} + \mathrm{e}^- + \bar{\nu}_\mathrm{e} \quad . \tag{2.2}$$

He was the first who named this particle “neutrino”. Soon after his publication H. Bethe and J. Perleis calculated the cross-section of a neutrino with a nuclei to be $\sigma = 10^{-44}\,\mathrm{cm}^2$, which corresponds to a mean free path of $10^{16}\,\mathrm{km}$ in solid matter [5]. This rather small cross-section let them believe it would be impossible to measure it. For two decades this assumption was right, until the “Project Poltergeist“ was build and run by C. L. Cowen and F. Reines in 1951. The goal of this project was to detect the anti-neutrinos which are produced in a nuclear fission reactors in inverse β-decays:

$$\bar{\nu}_e + p \rightarrow n + e^+ \quad . \tag{2.3}$$

Project Poltergeist consisted of a tank filled with 200 ℓ water and 40 kg cadmium chloride dissolved in it. While the protons of the water are targets for the neutrinos the cadmium absorbs the resulting neutron which is then excited and emits a γ-photon. The free positron annihilates with an electron whereby γ photons are created. While the electron-positron annihilation happens fast the absorption of the neutron is rather slow and takes a few microseconds which allows to distinguish signal from background, e.g. originating from the atmosphere or reactors.
In 1956 the project could finally observe free electron anti-neutrinos and confirm the calculated cross-section [6].
Six years later the existence of the ν_μ was proven by L. M. Lederman, M. Schwartz and J. Steinberger in the Brookhaven National Laboratory using a proton beam which was shot on a beryllium target [7]. With the discovery of the τ lepton a ν_τ neutrino was assumed and detected [8] with a similar experimental method as in Brookhaven in 2001.
All these experimental researches and discoveries in the 20th century lead to the development of the standard model of particle physics as it is known today. Consisting of 12 fermions, four gauge bosons and the Higgs boson it describes the strong, weak and electromagnetic interaction as well but not fully the gravitational interaction. The fermions are spin $^1/_2$-particles and are divided in three generations. Each generation includes two quarks, one with charge $+^2/_3$ and one with $-^1/_3$, as well as two leptons with charge -1 and neutral charge. For each fermion an anti-particle with opposite sign in charge exists. The three interaction forces are carried out by the four gauge bosons: W^+, W^-, Z^0 and γ. In 2012 the Higgs boson was discovered at the LHC which represents the quantum excitation of the Higgs-field, explaining why particles are massive [9].
The electric neutral neutrinos only interact weakly which processes are described through the gauge bosons $W^{+/-}$ and Z^0. The $W^{+/-}$ bosons only couple to left-handed fermions and right-handed anti-fermions. This leads to a maximum parity violation which confirms massless neutrinos. Out of Z^0 boson decay the number of existing neutrino generations can be derived. It can decay in every fermion-anti-fermion pair as long as the kinematics allow it. Comparing the theoretical calculated Z^0-resonance with the one measured will reveal the number of neutrino generations which was analyzed to be $N_\nu = 2.984 \pm 0.008$ [10].
The standard model as it is established today, describes most known physics well. However, there are still physical observations which are not explainable with it: the expansion of the universe, dark matter particles and neutrino oscillations.

2.2 The Phenomenon of Neutrino Oscillations

The idea of neutrino oscillation was first proposed by B. Pontecorvo in 1957 [11]. The initial theory described an oscillation between neutrino and anti-neutrino, however, an improved version of the neutrino oscillation theory was established describing an oscillation between the three neutrino flavors in the 1970's . In the following the discoveries, theory, and experiments concerning neutrino oscillations are described.

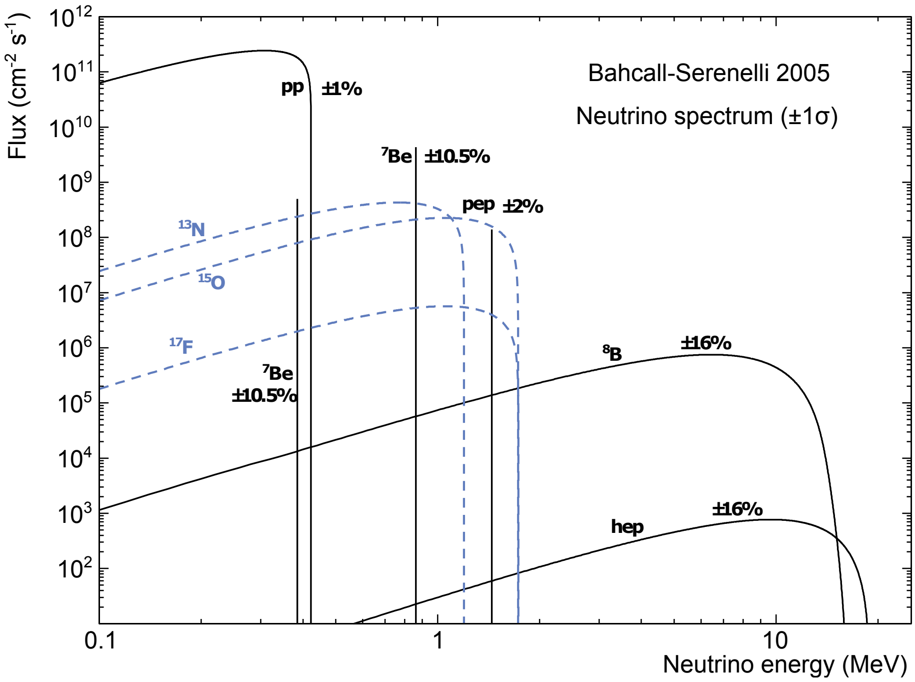

Figure 2.1: Illustrated is the solar neutrino flux generated by various fusion processes in the sun. The number given are the theoretical uncertainties as predicted by the solar standard model. Figure adapted from [17].

2.2.1 The Solar Neutrino Deficit

First indication of neutrino oscillation was discovered during the observation of solar neutrinos. The standard solar model (SSM) published by J. Bahcall in 1964 describes several fusion processes in the sun [12] creating neutrinos, the most dominant one is:

$$2e^- + 4p \rightarrow {}^4He + 2\nu_e + 26.73\,MeV. \tag{2.4}$$

With their small cross section neutrinos are regarded as the idle particles in order to reveal the processes in the sun, since their mean free path is larger than the dimension of the sun. A total energy spectrum of observable neutrinos is shown in figure 2.1. With the proposal of the Homestake experiment R. Davis made the first attempt to verify the calculated neutrino flux expected from the sun in the same year as the SSM was published.
The Homestake experiment, located in South Dakota, relies on the principle of the inverse β-decay of chloride [13]:

$$\nu_e + {}^{37}Cl \rightarrow {}^{37}Ar + e^- \tag{2.5}$$

with a threshold of $E_{thres} = 814\,keV$. Analyzing taken data revealed unexpected results: only one third of the predicted neutrinos flux was measured [14]. This solar neutrino deficit was also approved by other experiments such as GALLEX [15] or GNO [16], both too based on radiochemicals. The Kamiokande experiment using a grand tank filled with water confirmed previous observations of a solar neutrino deficit via Cherenkov light of electrons, which is induces by neutrinos passing through.

First theories on neutrino oscillation were already made by B. Pontecorvo in the 1960's allowing a flavor change ($\nu_e \rightarrow \nu_\mu$) on the path between the sun and the

detector [11, 18]. Previous mentioned experiments were only sensitive to electron neutrinos, hence, leaving the solar neutrino problem unsolved.
Finally, the Sudbury Neutrino Observatory (SNO) experiment, located in Ontario, Canada was able to verify the solar neutrino flux [19]. Using a tank of 1000 t heavy water it was the first experiment which was not only sensitive to electron neutrinos via the charged current (CC) but also to muon and tauon neutrinos via neutral current (NC) and elastic scattering (ES) processes:

$$\nu_e + \mathrm{d} \rightarrow \mathrm{p} + \mathrm{p} + \mathrm{e}^- \quad \text{(CC)}, \tag{2.6}$$
$$\nu_x + \mathrm{d} \rightarrow \mathrm{p} + \mathrm{n} + \nu_x \quad \text{(NC)}, \tag{2.7}$$
$$\nu_x + \mathrm{e}^- \rightarrow \nu_x + \mathrm{e}^- \qquad \text{(ES)}, \tag{2.8}$$

with $\mathrm{x} = \mathrm{e}, \mu, \tau$. Results showed a similar electron neutrino flux as measured by previous experiments. However, the determined flux of all neutrino flavors verified the proposed flux by the SSM [20].

2.2.2 Theory of Neutrino Oscillation

Pontecorvo was the first who predicted the possibility of the neutrino flavors not being the eigenstates of the particles itself. This observations were based on of kaon oscillations where particle and anti-particle transform into each other ($\mathrm{K}^0 \leftrightarrow \bar{\mathrm{K}}^0$) due to quark flavor oscillations [21]. At a later point, this theory was transfered to neutrino flavor oscillations [18, 22].

Analogous to the Cabibbo-Kobayashi-Maskawa (CKM) matrix for the mixing of quark flavors based on different weak- and mass eigenstates a matrix for the mixing of neutrino flavors was found. It is based on non-identical flavor- $|\nu_\alpha\rangle$ and mass- $|\nu_\mathrm{i}\rangle$ eigenstates ($\alpha = \mathrm{e}, \nu, \tau$ and $\mathrm{i} = 1,2,3$). Both are connected via a 3×3 mixing matrix U:

$$|\nu_\alpha\rangle = \sum_\mathrm{i} \mathrm{U}_{\alpha,\mathrm{i}} \, |\nu_\mathrm{i}\rangle \, . \tag{2.9}$$

The matrix was introduced by Maki, Nagakawa and Sakata (PMNS-matrix) in 1962 and is adapted from previous research of Pontecorvo. It describes the flavor mixing based on three mixing angles Θ_{23}, Θ_{13}, Θ_{12} and a CP violating phase δ used for parametrization:

$$\begin{pmatrix} 1 & 0 & 0 \\ 0 & \mathrm{c}_{23} & \mathrm{s}_{23} \\ 0 & -\mathrm{s}_{23} & \mathrm{c}_{23} \end{pmatrix} \cdot \begin{pmatrix} \mathrm{c}_{13} & 0 & \mathrm{s}_{13} e^{-\mathrm{i}\delta} \\ 0 & 1 & 0 \\ -\mathrm{s}_{13} e^{-\mathrm{i}\delta} & 0 & \mathrm{c}_{13} \end{pmatrix} \cdot \begin{pmatrix} \mathrm{c}_{12} & \mathrm{s}_{12} & 0 \\ -\mathrm{s}_{12} & \mathrm{c}_{12} & 0 \\ 0 & 0 & 1 \end{pmatrix} \tag{2.10}$$

with $\mathrm{s}_{ij} = \sin\Theta_{ij}$ and $\mathrm{c}_{ij} = \cos\Theta_{ij}$ whereby the matrix itself is split into three parts according to the mixing angles. Neutrinos produced at a time $\mathrm{t} = 0$ are in a pure flavor eigenstate. As the neutrino propagates on one-dimensional path the time-evolution of the mass eigenstate is given by a plane wave (in the following natural units are used):

$$|\nu_\mathrm{i}(t)\rangle = e^{-\mathrm{i}\mathrm{E}_\mathrm{i} t} \, |\nu_\mathrm{i}\rangle \tag{2.11}$$

Hence, a flavor eigenstate at a later time $\mathrm{t} > 0$ is described by:

$$|\nu_\alpha(t)\rangle = \sum_\mathrm{i} \mathrm{U}_{\alpha,\mathrm{i}} e^{-\mathrm{i}\mathrm{E}_\mathrm{i} t} \, |\nu_\mathrm{i}\rangle = \sum_{\mathrm{i},\beta} \mathrm{U}_{\alpha,\mathrm{i}} \mathrm{U}^*_{\beta,\mathrm{i}} e^{-\mathrm{i}\mathrm{E}_\mathrm{i} t} \, |\nu_\beta\rangle \, . \tag{2.12}$$

The probability for a neutrino of the flavor ν_α to transform into a flavor ν_β is then given by:

$$P_{\nu_\alpha \to \nu_\beta}(t) = |\langle \nu_\beta(t)|\nu_\alpha(t)\rangle|^2 = \sum_{i,j} U_{\alpha,i} U^*_{\beta,i} U^*_{\alpha,j} U_{\beta,j} e^{-i(E_i - E_j)t}. \tag{2.13}$$

For ultra-relativistic neutrinos ($p_i \gg m_i$ and $E \approx p_i$) this equation 2.13 can be simplified to:

$$P_{\nu_\alpha \to \nu_\beta}(L/E) = \sum_{i,j} U_{\alpha,i} U^*_{\beta,i} U^*_{\alpha,j} U_{\beta,j} e^{-i\frac{\Delta m^2_{ij} L}{2E}}. \tag{2.14}$$

The baseline length L hereby represents the distance between source and detector and E the energy of the neutrino. $\Delta m^2_{i,j}$ holds information about the difference of the squared masses of the neutrino mass eigenstates. This equation allows to estimate the supposed distance between the source and the detector depending on neutrino energy, mass differences and mixing angles in order to measure the appearance or disappearance of neutrino flavors.

2.2.3 Neutrino-Oscillation Experiments

To observe the neutrino flux and oscillation in general the experiments can be divided into two different techniques. First experiments were based on radiochemical techniques as used in the Homestake experiment by Davis which makes use of the inverse β-decay. An improvement of this experiment type was achieved by GALLEX or GNO due to the lower energy threshold of the transformation of gallium to germanium. On the other hand, the technique firstly used by SNO depends on a large tank filled with heavy water. This enables the observation of all three neutrino flavors in real-time via Cherenkov light and gives further insight on neutrino oscillation for energies larger than 1.9 MeV. An aspect which has to be taken into account when measuring the Θ_{12} and Δm^2_{12} is the influence of matter on the ν_e due to the presence of electrons in matter. This is the so-called MSW-effect introduced in the 1970's and 1980's [23]. The different mixing angles can be determined by measuring neutrinos of various sources.

Cosmic rays with energies in the GeV range induce a large number of particles with twice as much muon neutrinos than electron neutrinos both too with energies in the GeV range. The Super-Kamiokande experiment located in Japan makes use of a large tank filled with 50 kt ultra-pure water and 11 000 photomultipliers attached on the tank walls. This setup allows to investigate the up-down symmetry or asymmetry of ν_μ and μ_e as a function of distance through matter via Cherenkov light. The great advantage of such a measurement principle is the real-time distinguish ability for ν_μ and μ_e. Results show a ν_μ deficit as an up-down asymmetry regarding the atmospheric neutrino flux. Furthermore, with a measurable ν_τ flux this deficit was confirmed. With the Super-Kamiokande and Ice-Cube [24, 25] experiment the Θ_{23} mixing angle as well as the squared mass difference Δm^2_{23} are well studied parameters of the neutrino mixing.

Another source of a large neutrino flux are nuclear power plants with $\Phi_{\bar{\nu}_e} = 2 \cdot 10^{20}\,\mathrm{s}^{-1}$. Reactor neutrinos have energies of a few MeV. With a baseline length of 1 km to 2 km detectors are then able to measure the scale of Θ_{13} and Δm^2_{13}. Experiments like Daya Bay (China) and Double Chooz (France) make use of a combination of two

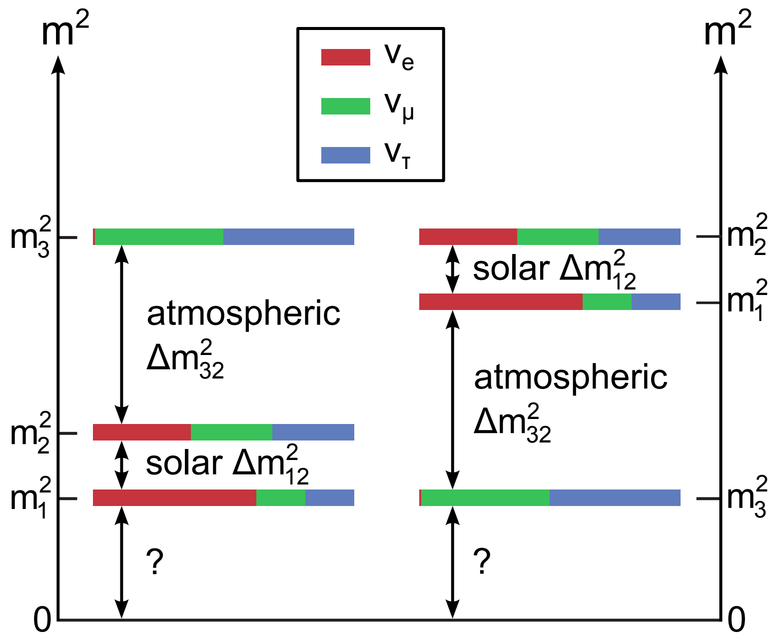

Figure 2.2: The normal and the inverted mass hierarchy are shown with the flavor fractions indicated by colored bars. The absolute mass scale can not be derived by the current oscillation experiments. Figure adapted from [26]

detectors, one directly next to the neutrino source, the other at the baseline length measuring the disappearance of $\bar{\nu}_e$.

The sign of Δm^2_{32} could not yet be determined by the current neutrino oscillation experiments and, further, the absolute mass scale can not be measured by them. However, current results allow to three scenarios for the total neutrino mass eigenstates:

- normal mass hierarchy: $m_1 < m_2 \ll m_3$
- inverted mass hierarchy $m_3 \ll m_1 < m_2$
- quasi-degenerated case with $m_1 \approx m_2 \approx m_3 \gg 10^{-3}\,\mathrm{eV}$

Figure 2.2 illustrates the first two scenarios whereby the individual flavor eigenstates are indicated in colored bars. However, for the absolute mass scale the neutrino mass has to be measured directly.

2.3 Experimental Approaches to Measure the Neutrino Rest Mass

Previously described neutrino oscillation experiments are unable to measure the total mass scale of the neutrino mass eigenstates. In order to determine these masses different approaches are possible which can be divided in model-dependent and model-independent ones. The most noticeable approaches are described shortly in the following.

Cosmology
Satellites in earths' orbit, such as the Planck satellite, measure the anisotropies in

the temperature of the cosmic microwave background (CMB). The CMB exists due to the expansion of the universe which forced the decoupling of photons from matter about 380 000 years after the Big Bang. According to this, the decoupling of neutrinos from matter leave a cosmic neutrino background. These so-called relic neutrinos have very low energies and in combination with their small cross section experiments were not yet able to detect them. The cosmological model estimates a density Ω_ν for the relic neutrinos of $336\,\mathrm{cm}^{-3}$. Comparing this to the total energy density of the universe Ω_{tot} it yields to a total mass for all three neutrino mass eigenstates of:

$$\sum_k m_k = 93\Omega_\nu h^2 \mathrm{eV}, \tag{2.15}$$

whereby h is the dimensionless Hubble parameter. With latest achieved results a model-dependent upper limit for all neutrino mass eigenstates is derived to [27]:

$$\sum_k m_k \leq 0.23\,\mathrm{eV}. \tag{2.16}$$

Double β-Decay

Nuclei with an even mass number can have an equal number of neutrons and protons in even-even or odd-odd configuration. For some of these nuclei the single β-decay is energetically forbidden and the rare double β-decay ($2\nu\beta\beta$) becomes observable. In this decay two protons or two neutron decay simultaneously:

$$2n \rightarrow 2p + 2e^- + 2\bar{\nu}_e \tag{2.17}$$

$$2p \rightarrow 2n + 2e^+ + 2\nu_e. \tag{2.18}$$

In 1937 E. Majorana published his theory of the neutrino being its own antiparticle, which is theoretically allowed since they do not carry charge. As a consequence, the possibility of a neutrinoless double β-decay ($0\nu\beta\beta$) exists when the neutrino is emitted and absorbed within the nucleus. The corresponding Feynman diagram is shown on the left side in figure 2.3 and the expected energy spectrum on the right. Experiments such as GERDA [28] and MAJORANA [29] are searching for this decay but have not yet succeeded. The half life $T^{0\nu\beta\beta}_{1/2}$ is an important parameter for these experiments and is given by:

$$\left(T^{0\nu\beta\beta}_{1/2}\right)^{-1} = G^{0\nu\beta\beta}\left(Q_{\beta\beta}, Z\right) \cdot |M^{0\nu\beta\beta}_{GT} - \left(\frac{g_V}{g_A}\right)^2 M^{0\nu\beta\beta}_{F}|^2 \cdot \frac{\langle m_{\beta\beta}\rangle^2}{m_e^2}, \tag{2.19}$$

whereby $G^{0\nu\beta\beta}$ is the phase space factor, $Q_{\beta\beta}$ the endpoint energy, Z the atomic number of the decaying isotope, $M^{0\nu\beta\beta}_{GT}$ and $M^{0\nu\beta\beta}_{F}$ the respective Gamov-Teller and Fermi matrix elements and g_V and g_A represent the axial and vector coupling constants. $\langle m_{\beta\beta}\rangle$ is the coherent sum of the effective Majorana neutrino mass given by $\langle m_{\beta\beta}\rangle = |\sum_{i=1}^{3} U_{ei}^2 \cdot m_i|$ and m_e the electron mass. Equation 2.19 is applicable for purely left-handed V-A weak currents and light massive Majorana neutrinos. If observed, the double β-decay will give information about whether the neutrino can be a Majorana particle and, further, a model-dependent value for the neutrino mass. However, with a lower boarder of the half life of $T^{0\nu\beta\beta}_{1/2} \geq 2.1 \cdot 10^{23}$ a an upper limit of $\langle m_{\beta\beta}\rangle$ is estimated to:

$$\langle m_{\beta\beta}\rangle < (0.2 - 0.4)\,\mathrm{eV}. \tag{2.20}$$

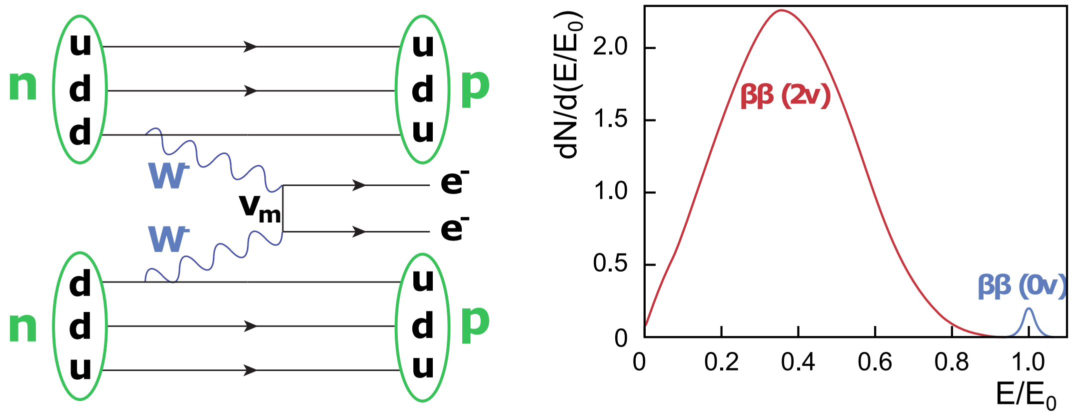

Figure 2.3: Double β-decay: On the left side the Feynman diagram of the neutrinoless double β-decay is shown. Due to the exchange of virtual neutrinos only two electrons are emitted by the nucleus. On the right side the energy spectrum is displayed. The spectrum is scaled by a factor 1 (0.2) for the $2\nu\beta\beta$ ($0\nu\beta\beta$) decay. Figures adapted from [30, 31].

Single β-Decay

Measuring the energy spectrum of the single β-decay close to its kinematic endpoint energy E_0 gives a model-independent $\bar{\nu}_e$ mass. The energy spectrum of the three-body-decay:

$$n \rightarrow p + e^- + \bar{\nu}_e, \tag{2.21}$$

is illustrated on the right in figure 2.4 and the corresponding Feynman diagram on the left. Electrons with energies close to E_0 hold information on non-relativistic neutrinos and give the effective neutrino mass if measured precisely. The energy spectrum is given by Fermi's Golden Rule [32] as follows:

$$\begin{aligned}\frac{d^2N}{dEdt} = C \cdot F\left(E, Z+1\right) \cdot p_e \cdot \left(m_e c^2 + E\right) \cdot \left(E_0 - E\right) \\ \cdot \sqrt{\left(E_0 - E\right)^2 - m_{\nu_e}^2 c^4} \cdot \Theta\left(E_0 - E - m_{\nu_e} c^2\right),\end{aligned} \tag{2.22}$$

containing Fermi's coupling constant G_F, the Cabbibo angle Θ_C, the Fermi function F and the momentum p_e, mass m_e and energy E of the emitted electron. The constant C is given by:

$$C = \frac{G_F^2 \cos^2\Theta_C}{2\pi^3 c^5 \hbar^7} \cdot |M|^2, \tag{2.23}$$

with a hadronic matrix element M. E_0 is hereby the theoretical endpoint energy for a massless neutrino. A non-zero effective mass m_{ν_e} pushes the actual endpoint energy to a lower value (illustrated in the zoom-in in figure 2.4).

The Mainz [33] and Troitsk [34] experiments measured the endpoint energy. With this model-independent method the best limits are achieved up to now [35]:

$$m_{\nu_e} < 2.0\,\mathrm{eV}\ (95\%\ \mathrm{C.L.}). \tag{2.24}$$

Limits are dependent on systematic uncertainties as well as restricted source statistics. As a next generation experiment KATRIN, on site in Karlsruhe at Campus North of the Karlsruhe Institute of Technology, aims to measure the effective neutrino mass in the sub-eV regime surpassing previous experiments by one order of magnitude.

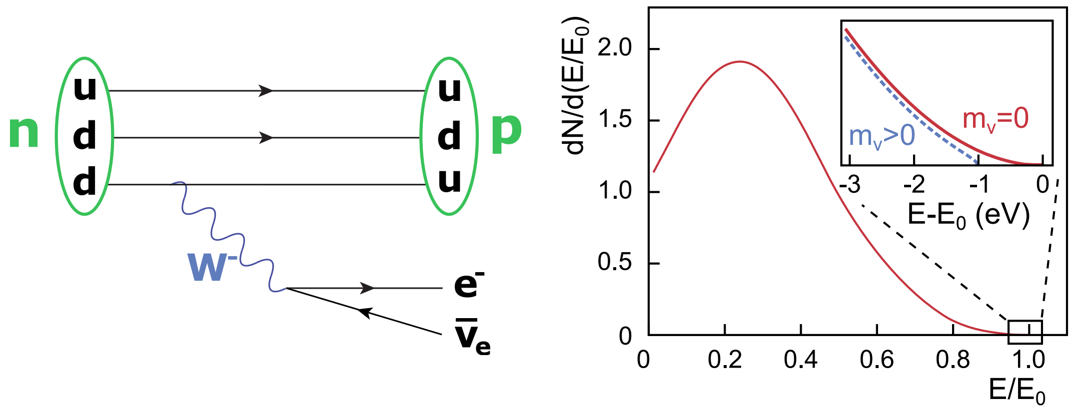

Figure 2.4: Single β-decay: On the left side the Feynman diagram is displayed. A neutron transforms into a proton while emitting a W^- boson which eventually decays into an electron and a neutrino. The right side shows the corresponding energy spectrum of the single β-decay. A zoom-in shows the endpoint of the energy spectrum with a neutrino mass of 1 eV (blue dashed line) in comparison to a vanishing neutrino mass (solid red line). Figures adapted from [30].

3. The KATRIN Experiment

The **Ka**rlsruhe **Tr**itium **N**eutrino experiment (KATRIN), located in Karlsruhe, Germany aims to determinate the mass of the electron anti-neutrino through precise measurement of the kinematics of the tritium β-decay. With a sensitivity of 200 meV/c^2 it will improve the current neutrino mass sensitivity given by previous experiments by one order of magnitude. The KATRIN collaboration consists of several institutes and universities spread all over the world with significant contribution from Germany and USA.

In this chapter the KATRIN measurement principle using a MAC-E filter (section 3.1) as well as the main components (section 3.2) and the measurement phases of the spectrometer and detector section (SDS) system (section 3.3) are described.

More details on the KATRIN experiment and its components are given in the [36].

3.1 The MAC-E Filter Principle

To determine the mass of the neutrino the KATRIN experiment will investigate the tritium β-spectrum close to the endpoint energy $E_0 = 18.6\,\mathrm{keV}$ with high precision. Therefore KATRIN utilizes the measurement principle of a Magnetic Adiabatic Collimation combined with an Electrostatic (MAC-E) filter [37]. This principle combines electric and magnetic fields, shown in figure 3.1. The β-decay electrons are guided by the magnetic field, provided by superconducting solenoids along the beamline, adiabatically through a spectrometer towards the detector. The electric field, parallel to the magnetic field, is provided by applying (negative) high voltage on the spectrometer vessel forming a potential barrier U_0 for incoming electrons. To overcome this barrier the electrons require a longitudinal energy of $E_{||} \geq e{\cdot}U_0$. The potential U_0 can be varied in order to scan the energy spectrum of the electrons in an integral way. In β-decay electrons are emitted isotropically and, hence, posses a transverse energy component $E_\perp$ as well. In order to use most of the source luminosity and to increase statistics at the endpoint E_0 of the energy spectrum while at the same time measuring the full kinetic energy of the electrons, the transverse energy is transformed into longitudinal energy. This is implemented through varying the magnetic field strength along the electron trajectories within the spectrometer. To fulfill the following relation of the magnetic momentum μ of the electrons

$$\mu = \frac{E_\perp}{B} = \mathrm{const} \tag{3.1}$$

the magnetic field has to vary slow enough (adiabatically). This equations concludes that the transverse energy component is minimal when the magnetic field is at its minimum. Hence at B_{min} is the analyzing plane of the spectrometer where the potential should be highest.

Another effect coming with the MAC-E filter is the magnetic mirror effect, where electrons guided from a weak into a strong magnetic field are reflected due to a turnover of their momentum vector. In order to be reflected the electrons emitted in the source must exceed the maximum polar emission angle Θ_{max} of:

$$\Theta_{max} = \arcsin\left(\sqrt{\frac{B_S}{B_{max}}}\right) \tag{3.2}$$

where B_S is the magnetic field at the source and B_{max} the maximum field along the electrons trajectories. In the KATRIN experiment B_{max} is provided by the pinch magnet which is located between the main spectrometer and the detector section. The induced background of multiple reflected electrons is analyzed and discussed in [38].

At the analyzing plane the magnetic field is at its minimum, but still non-zero, meaning the conversion of transversal into longitudinal energy is not perfect. As a consequence the kinetic energy is not analyzed correctly by the MAC-E filter. This results in an energy resolution for the KATRIN spectrometer of

$$\Delta E = \frac{B_{min}}{B_{max}} \cdot E_{kin} \quad . \tag{3.3}$$

3.2 Main Components

The KATRIN experiment with a beamline length of about 70 m consists of several components all shown in figure 3.2. Electrons emerging from tritium β-decay in the windowless gaseous tritium source (section 3.2.1) are guided magnetically through the transport section (section 3.2.2). In the spectrometer and detector section the electron energy is analyzed before they impinge onto the focal-plane detector (section 3.2.3).

3.2.1 Windowless Gaseous Tritium Source

Thewindowless gaseous tritium source (WGTS), shown in (B) in figure 3.2, consists of a 10 m long stainless steel tube with a diameter of 9 cm. Gaseous molecular tritium is injected at the center of this beam tube. The injection rate has to be highly stable in order to reduce turbulences, realized by injecting tritium through a set of capillaries with an inlet pressure of 10^{-3}mbar [41]. This setup allows the system to achieve a column density of $\rho d = 5 \cdot 10^{17}$ molecules/cm^{-2} which complies with an activity of $\approx 10^{11}$Bq [36]. On both sides of the WGTS several turbo molecular pumps (TMPs) reduce the tritium flow by a factor of 100 which reduces energy loss of the β-electrons by scattering off tritium molecules. The pumped out tritium is re-furbished in an inner loop cycle before it is re-injected [41]. The whole WGTS is operated at 30 K by using a novel two-phase neon cooling system [42], which has to be retained with high stability (±3 mK) in order to minimize Doppler-broadening caused by thermal fluctuations [43]. To keep the tritium purity on a constant level of >95% it is constantly monitored by a Laser Raman spectroscopy system (LARA) [44].

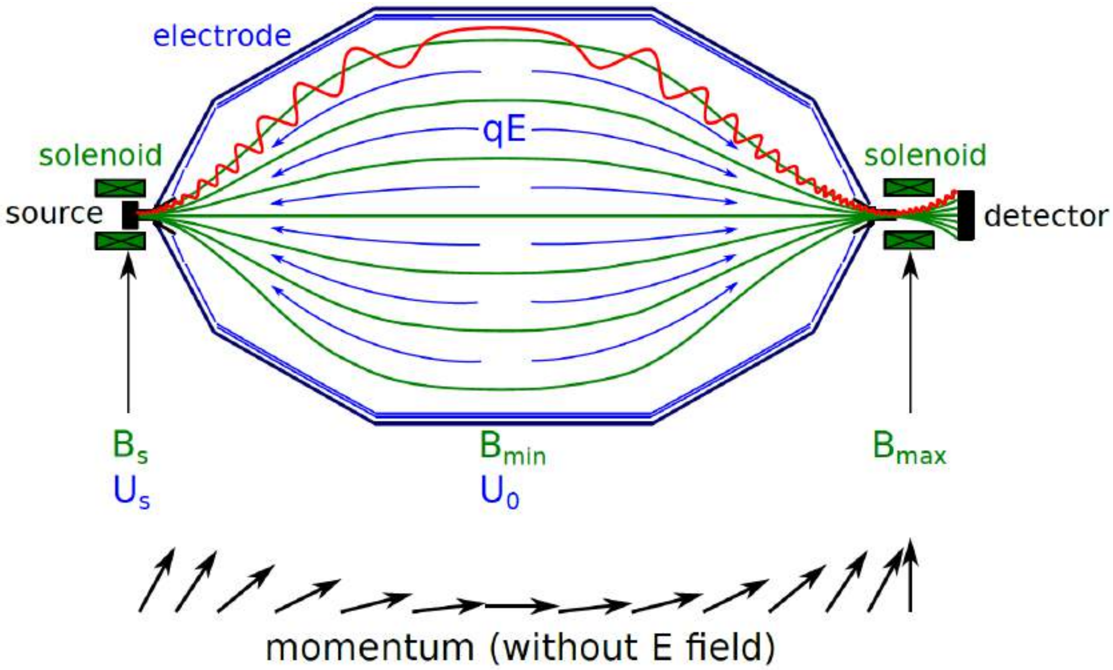

Figure 3.1: Draft of the MAC-E filter principle. Electrons emitted isotropically in the source follow the magnetic field lines (green) with a cyclotron motion (red). The magnetic field is provided by two superconducting solenoids each on one side of the spectrometer. In the spectrometer the electrons are energetically filter by applying an electric field (blue). Only those electrons overcoming this barrier U_0 impinge on the detector. The black arrows below the drawing indicate the direction of the electron's momentum. Figure adapted from [39].

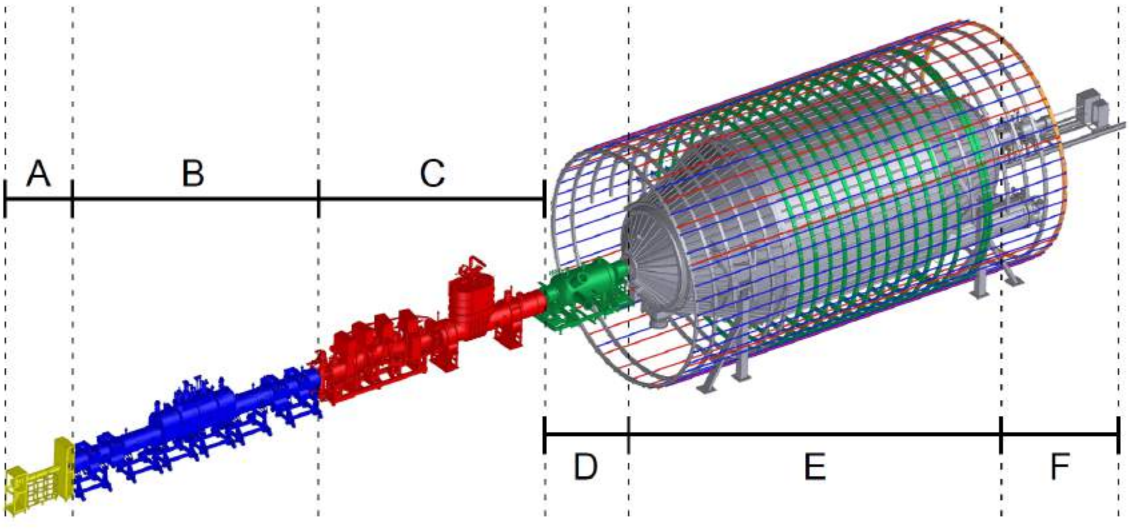

Figure 3.2: Overview of KATRIN beamline. The experiment consist of several components, all together forming a 70 m long beamline: (A) The rear section monitors the activity in the WGTS (B) where the electrons are emitted by β-decay of tritium. These electrons are guided adiabatically along a magnetic flux tube through the transport section (C). In the pre-spectrometer (D) and main-spectrometer (E) the electrons are filtered energetically and if passing the latter, are detected by the focal-plane detector system (F). Figure adapted from [40].

The β-electrons are adiabatically guided in a magnetic field of $B_S = 3.6\,\mathrm{T}$ provided by several superconducting solenoids surrounding the beam tube. Only a small part of the isotropically emitted β electrons contribute to the endpoint E_0 of the energy spectrum. To increase the number of analyzable electrons the β-decay is within a magnetic field, allowing to analyze all β-electrons with a starting polar angle of $<\Theta_{\mathrm{max}}$.

Mounted on the upstream side of the WGTS is the rear section. Its task is to control and monitor the activity within the WGTS: the electric potential of the tritium plasma, and the column density of the tritium gas.

3.2.2 Transport Section

The KATRIN transport section, as the name implies transports the electrons from the WGTS to the Spectrometer and Detector Section (SDS). Its primary goal is to reduce the tritium flow between the source and the SDS by 14 orders of magnitude while at the same time the β-electrons are guided adiabatically. Along the $\approx 14\,\mathrm{m}$ of its beamline the tritium flow is reduced to $<10^{-14}\,\mathrm{mbar} \cdot {}^{l}\!/_{s}$ to prevent tritium molecules from entering the SDS components. If these molecules decay within the spectrometers they would induce an increase of the background level.
The transport section consists of into two sub-components: The differential and the cryogenic pumping section.

Differential Pumping Section (DPS)
The DPS, shown on the left in figure 3.3, is located directly on the downstream side of the WGTS. It consist of five superconducting solenoids which can provide nominal fields up to $B_{\mathrm{CPS}} = 5.6\,\mathrm{T}$ and in total six TMPs, four are each in between two solenoids, the other two are on the upstream end. The DPS is arranged in two 20°-chicanes to increase the pumping efficiency of the TMPs. With this setup, the DPS is able to reduce tritium flow in total by five orders of magnitude. The pumped out tritium is then fed back for reuse in the source section via an outer loop circuit [45].

Besides electrons, ions as well result from the β-decay and are guided towards the spectrometer, where the would induce a large background when entering. To identify ion species and preventing them from entering the SDS section three different subsystems are installed along the DPS: An FT-ICR diagnostic unit identifies the ion species by making use of the Fourier-transformation of the cyclotron signals inside a Penning trap (during specific measurements) [46, 47]. To prevent identified ions a ring-shaped blocking electrode, located at the downstream en of the DPS, is put on a blocking potential of $+100\,\mathrm{V}$. Furthermore, three dipole electrodes installed within the DPS are able to deflect ions onto the walls on the beam tube by using an $\vec{\mathrm{E}} \times \vec{\mathrm{B}}$ drift. This drift further prevents the built-up of a positive space charge along the beam tube [48, 49].

Cryogenic Pumping Section (CPS)
The CPS connects to the downstream side of the DPS and is shown on the right side of figure 3.3. It is the last component in the beamline which is allowed to hold a significant amount of tritium. Its pumping technique is based on adsorption of tritium gas on argon frost. The beam tube is therefore cooled down to $4.5\,\mathrm{K}$ by

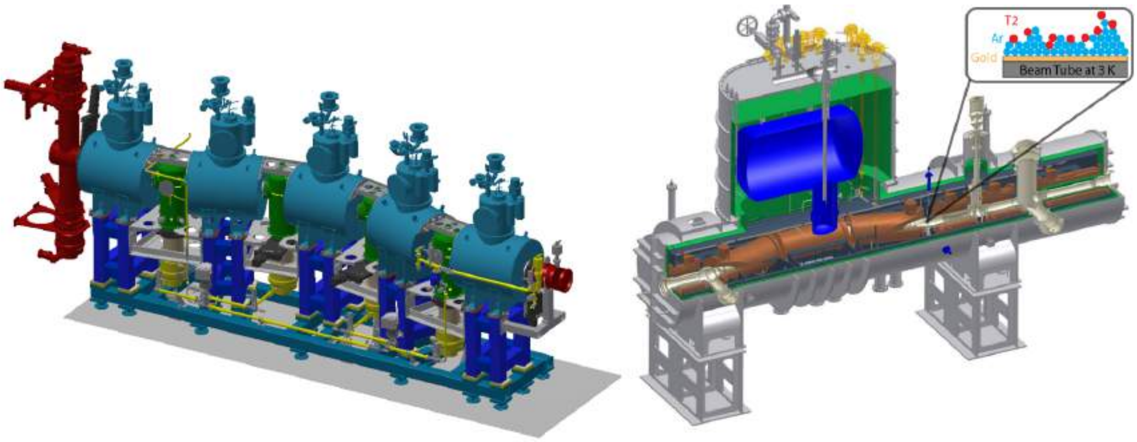

Figure 3.3: Components of the KATRIN transport section.
Left: The Differential Pumping Section (DPS). It consists of five superconducting solenoids (dark cyan) and six turbo molecular pumps, four in between the magnets (cyan) and two on the upstream end (red). These parts are aligned along two 20° chicanes reducing the tritium flow in total by five orders of magnitude. Figure adapted from [50].
Right: The Cryogenic Pumping Section (CPS). Consisting of seven superconducting solenoids aligned in two 15° chicanes the CPS uses argon frost to accumulate tritium on the inner surface of the beam tube via cryosorption (red). With this method the tritium flow is further reduced by seven orders of magnitude. Figure adapted from ([39]).

liquid helium in order to maintain an argon frost layer on its inner surface. The CPS has to be regenerated every 60 days and the accumulated tritium is pumped out of the system and fed back into the tritium cycle. For regeneration the beam tube is warmed up to 100 K and flushed with warm helium gas. Afterwards the argon frost layer is renewed. The trapping efficiency of tritium is increased by arranging the beam tube in two 15°-chicanes so the tritium molecules have no direct line of sight to the spectrometers [51]. Overall this reduces the tritium flow by seven orders of magnitude.
For guiding the β-electrons to the SDS section seven solenoids are aligned along the beamline. Furthermore, the beamline is of the CPS is equipped with a condensed krypton source and a beam monitoring detector which can be moved in and out of the beamline without breaking the vacuum [52].

3.2.3 Spectrometer and Detector Section

On the downstream side of the transport section the tritium-free spectrometer and detector section (SDS) is located. It consists of two electrostatic retarding spectrometers using the MAC-E filter principle described in section 3.1 and a Focal-Plane-Detector (FPD) system described in detail in section 4. The efficient reduction of the tritium flow in the transport section results in a low background generated by β-decays of tritiated particles. For further minimization of background rate the spectrometers operate at pressures in the ultra high vacuum (UHV) regime at about 10^{-11} mbar in order to avoid background induced by scattering effects of β-electrons with residual gas.

Pre-Spectrometer

The pre-spectrometer (PS), shown (D) in figure 3.2, is a vacuum vessel with 3.4 m length and 1.7 m diameter [36]. The magnetic field for its MAC-E filter is provided by two superconducting solenoids PS1 and PS2, one on each side of the spectrometer. Operating the solenoids at a nominal field of 4.5 T results in an energy resolution of $\Delta E \approx$70 eV for electrons with an energy of E_0 = 18.6 keV. The PS can be used as a pre-filter for low-energy electrons of the tritium β-decay and, thus, reduce the electron flux entering the main-spectrometer by seven orders of magnitude. A reduced electron flux further reduces the background induced by scattering of β-electrons off residual gas and is advantageous for the detector which cannot handle rates larger than $10^{6}\,{}^{e^-}/_{s}$. One issue which arises and has to be taken into account when operating the PS at high voltages is the creation of a large penning trap [53] between the pre- and main-spectrometer. This has to be "neutralized" in order to prevent a major background.

Main-Spectrometer

The main spectrometer (MS), shown in (E) figure 3.2, is a large stainless steel vessel 23 m in length with a maximal diameter of 10 m. The two solenoids providing the magnetic field for its MAC-E filter are the PS2 on its upstream side, which it shares with the pre-spectrometer, and the pinch magnet (PCH) on the downstream side which is part of the detector system. The PCH magnet provides the strongest magnetic field of B_{PCH} = 6 T in the whole KATRIN beamline. With a minimal magnetic field of B_{min} = 0.3 mT in the analyzing plane of the MS this results in an energy resolution of ΔE= 0.93 eV at an electron energy of E_0 = 18.6 keV [36]. For fine-tuning the magnetic field inside the MS its vessel is surrounded by a system of air-coils [54]. To fine-shape the electric field inside the spectrometer a two-layer wire electrode is installed on its inner surface.

Another advantage of these wire electrode is it keeps the low-energy electrons emitted from the inside surface of the vessel from entering the sensitive volume of spectrometer. The retarding potential of this spectrometer is variable and, hence, able to scan the energy spectrum close to the endpoint E_0 (so-called tritium scanning mode, scans an energy interval of E_0 - 30 eV to E_0 + 5 eV).

Focal-Plane Detector

The last component of the KATRIN beamline is the Focal-Plane Detector (FPD). It is located on the downstream side of the main-spectrometer and counts the electrons which pass the MAC-E filter. Only a few signal electrons per second are expected during measurements with tritium, but for calibration measurements the detector has to be able to measure rates of a few kHz. The whole FPD apparatus is described in more detail in chapter 4.

3.3 Measurement Phases of the Spectrometer and Detector Section

Two SDS measurement phases were already performed with FPD system and the main-spectrometer in tandem operation. The main goal of these campaigns was to

Table 3.1: Standard parameter settings of the FPD system during SDS-I commissioning phase [57]. Parameters L and G are described in section 4.6.

Parameter	Value
Pinch magnet field	5 T
Detector magnet field	3.5 T
PAE potential	10 kV
Shaping Length L	1.6 µs
Gap Length G	0.2 µs
MS Vessel Voltage	-18.5 kV
Wire Electrodes	-18.6 kV

characterize the system in terms of background and electron transmission.

SDS-I

The first measurement campaign was a 3-month commissioning phase which took place in mid 2013 [40, 55, 56, 57]. This was the fist time the FPD system and the main-spectrometer were operated together. The outcomes of this measurement phase resulted in several improvements for both hardware and software components [58, 59]. An example of relevance for this thesis is the wafer test board [60] which allows to test the resistance of adjacent pixels on the wafer prior its installation into the FPD system. This ensures for following measurement phases a fully working detector wafer. The for the SDS-I campaign used standard parameters settings of the FPD system are listed in table 3.1 (parameter L and G described in section 4.6). For specific measurements the settings applied to the SDS system were adjusted. Due to quenching problems of the pinch magnet the applied magnetic field strength was lowered to $B_{PCH} = 5\,T$ and $B_{DET} = 3.5\,T$ during the measurement phases. More details on the parameter settings and the results can be found in [57].

SDS-II

The SDS-II campaign was split in two sub-phases: SDS-IIa from October 2014 to March 2015 and SDS-IIb from June 2015 onwards to September of the same year [50, 38]. Prior to its installation the SDS-II wafer was tested with the newly developed test board and showed no shorts [61]. This was confirmed during the measurement phase. In order to avoid further quenching incidents of the pinch magnet the magnetic field was set to $B_{PCH} = 5\,T$ and $B_{DET} = 3\,T$ for this measurement campaign, other parameters were left unchanged as in table 3.1. Unfortunately, several pixels, all on the same installed preamplifier card, showed enormous temperature fluctuations during operation which made the measured spectra useless for further analysis and, as a consequence, were excluded further on. After the measurement phase had finished the preamplifier card was replaced. Analysis and further details can be found in [55, 50].

SDS-III

Starting in October 2016 a next measurement phase of the SDS system preliminary to the neutrino mass measurement is beginning. For the SDS-II campaign the whole KATRIN beamline is operated and tested for the first time.

4. The Focal-Plane Detector System

The Focal-Plane Detector system (FPD) located on the downstream side of the main spectrometer guides electrons onto the detector wafer and consists of several subsystems, listed in figure 4.1. The signal electrons follow the magnetic field provided by the magnet system described in section 4.1. Before impinging on the detector wafer the electrons can be accelerated as described in section 4.2. To minimize scattering of electrons with residual gas a suitable vacuum is needed which is provided by the vacuum system (see section 4.3). The FPD system houses a cooling system (see section 4.4) in order to cool the detector wafer (section 4.5), and its read-out electronics (section 4.6). A series of calibration sources allows to commission and characterize the detector prior to the data taking (see 4.7). To reduce the intrinsic background the wafer is surrounded by passive copper and lead shielding as well as a recently developed veto system described in section 4.8.

4.1 Magnet System

The FPD magnet system consists of two superconducting solenoids, the pinch (PCH) and detector (DET) magnet, which guide the signal electrons that passed the main spectrometer (MS) onto the detector wafer. The PCH magnet, located directly on the downstream end of the MS provides the maximum magnetic field strength in the whole KATRIN beamline of $B_{max} = 6\,T$. It is part of the MAC-E filter and is directly related to the energy resolution of the spectrometer according to equation (3.3). The detector magnet (DET), located further downstream, can too provides fields up to 6 T but is usually operated with $B_{DET} < B_{PCH}$. It surrounds the detector wafer. With those nominal fields the magnetic flux at the wafer is $210\,Tcm^2$. By operating the PCH magnet at a higher field than the DET magnet electrons that do backscatter from the detector wafer are prevented from re-entering the main-spectrometer where they would induce additional background. To reach the superconducting state both magnets are cooled down with liquid helium and are held at 4.2 K. This allows to switch the magnets in a persistent mode after initial ramp-up. To compensate the attractive force between the magnets of 54 kN [55] spreader bars are installed in between.

4.2 Post-Acceleration-Electrode

The Post-Acceleration-Electrode (PAE) is a full copper trumpet-shaped electrode with a thickness of 3 mm (shown in figure 4.2) located on the downstream side of the

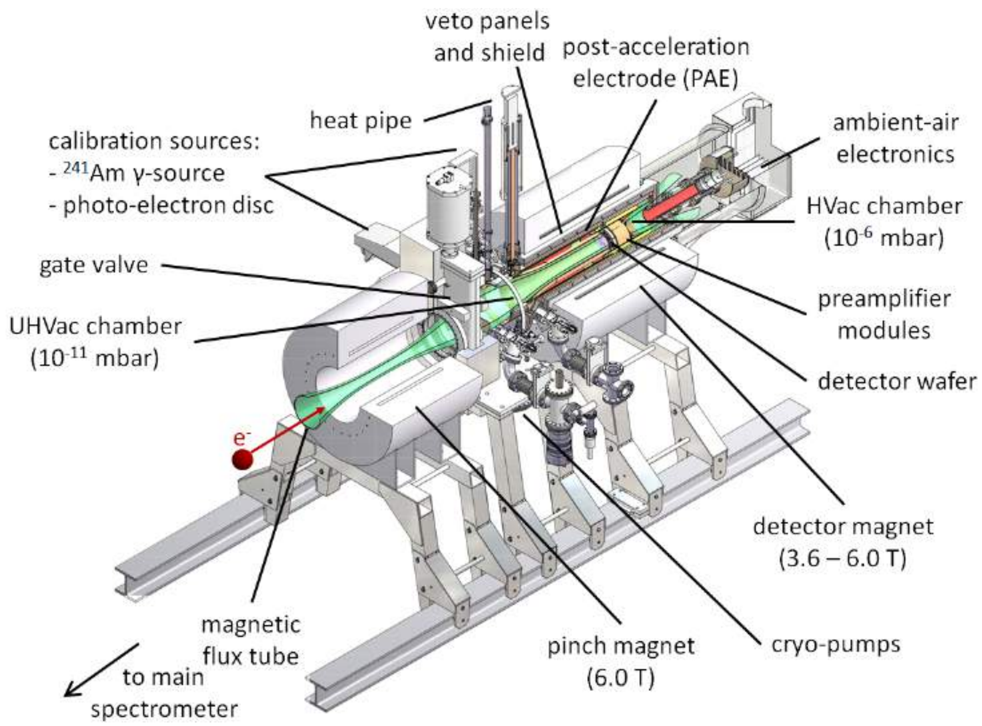

Figure 4.1: Schematic overview of the FPD system. It consists out of several different subsystems described in this chapter. Picture adapted from [62].

PCH magnet. On its upstream end it is connected to the grounded vacuum chamber through an insulating ceramic. The downstream side separates the ultra high vacuum chamber from the high vacuum chamber via a feedthrough flange on which the wafer and front-end electronics are mounted. Inside the high vacuum chamber three quartz tubes of different diameters with stainless steel foils on the out- and inside surface enclose the readout electronics. The inner electrodes are set to the same potential as the PAE whereas the outer are connected to the grounded vacuum chamber walls. This set up seals the high electric fields inside the insulators.
The PAE allows to accelerate the electrons which passed the MAC-E filter of the main spectrometer. This has two advantages: Firstly, it boosts the energy spectrum of the electrons to regions where the background induced by γ- and β-emitting nuclei close to the detector is smaller. Secondly, a post acceleration reduces the backscatter effects from the detector wafer by decreasing incident the angles of the electrons. This allows to operate the detector within higher magnetic field strengths [36].
Though designed for 30 kV the PAE can currently not be operated stable at voltages higher than 10 kV. To investigate the breakdown characteristics of the PAE at higher voltages a separate test apparatus was build with collaboration partners at the University of Washington in Seattle (see chapter 5).

4.3 Vacuum System

The FPD vacuum system consists of two nested chambers operated at different vacuum pressures: an ultra high (UHVac) at $1{\cdot}10^{-11}$ mbar and a high vacuum (HVac) chamber at $1{\cdot}10^{-6}$ mbar. The PAE which separates both chambers is designed to withstand the forces induced by pressure differences, even at greater pressure

Figure 4.2: Post-Acceleration-Electrode of the FPD system. Picture adapted from[63].

difference than between UHVac and HVac. The UHVac chamber is directly connected to the MS and houses the detector wafer. The HVac chamber which houses the cooled front-end electronics is mostly used for thermal insulation purposes. While both chambers are initially pumped on via turbo-molecular pumps the FPD system uses cryogenic pumps during standard operation within magnetic fields.
The lowest achievable pressure is dominated by outgassing rate of the stainless steel surfaces and electronics inside the chambers. The main gas in the UHVac chamber and both chambers are baked out prior connecting to the MS.

4.4 Cooling System

For reading out incoming signals from the wafer a series of different readout electronics are installed (see section 4.6). These electronics heat up while operated and therefore have to be cooled. Since they are located within the HVac chamber the cooling mechanism must be vacuum compatible. Therefore a custom made heat pipe schematically shown in figure 4.3 has been developed and installed. It is mounted on the upstream end of the PAE with its evaporator connected to the PAE ceramic.

It is a custom-made pipe shaped device using gaseous nitrogen which is cooled down until it liquefies at the condenser and finally drops down on the evaporator. For controlling the heat pipe cooling power several temperature sensors (RTDs) and a heater next to the condenser are used. The nitrogen VCR port leads to a nitrogen reservoir and the 50-pin feedthrough is used to electrically connect to the built-in electronics. At the evaporator the liquefied nitrogen evaporates again cooling the copper PAE, the detector wafer, and the front-end electronics installed at its downstream side (shown in figure 4.4).

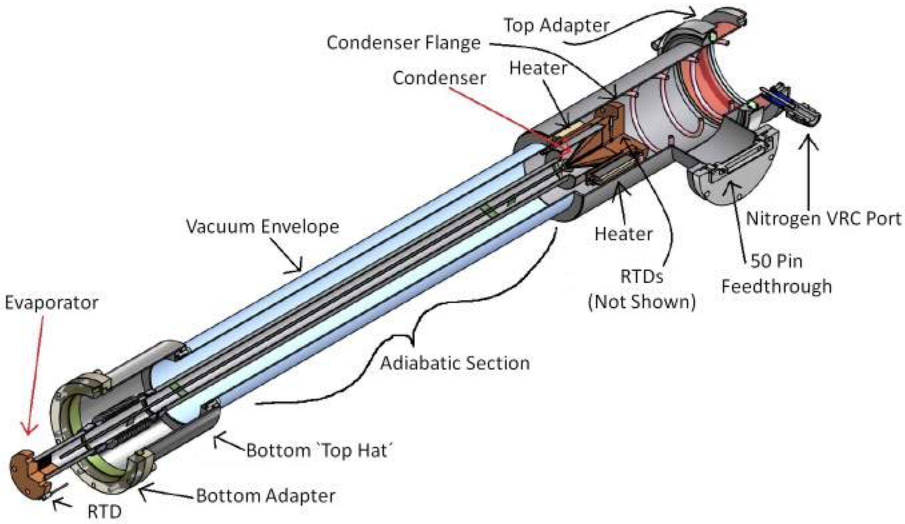

Figure 4.3: The heat pipe uses liquid nitrogen to cool down the electronics of the FPD system. Picture adapted from [64]

The temperature is regulated by the cooling power of the heat pipe which has a manually controlled temperature set point for the condenser. Depending on the temperature set point, the cooling power is adjusted. Thus, a lower set point results in a lower temperature at the detector wafer. However, this is limited by the fact that nitrogen freezes out if setting the temperature set point to a significant lower value than the freezing temperature of nitrogen in vacuum. If the liquid nitrogen freezes out at the evaporator the continuous cooling is interrupted resulting in a warm up of the detector electronics.

Having the evaporator at the upstream and the detector wafer at the downstream side of the PAE has the advantage of a stable or slow changing detector wafer temperature. Concerning the energy resolution a cooler detector wafer shows better results for various reasons: Firstly, with cooler read-out electronics the thermal noise becomes less. And secondly, the leakage current is smaller improving charge-collection properties since the charge-mobility is higher at lower temperatures (due to less lattice vibrations [65]). Since the temperature of the detector and the front-end electronics are coupled through the feedthrough flange it limits the achievable operating temperature to -40°C to + 70°C [55].

4.5 Detector Wafer

The FPD consists of a monolithic silicon PIN-diode wafer of 500 µm thickness and a diameter of 125 mm. Electrons impinge on its n-doped front side covering an area of 90 mm in diameter with an intrinsic dead-layer of 100 nm. On its backside the wafer is segmented into 148 pixel each covering an area of about 44 mm^2 which are separated by an isolating layer of 55 µm width resulting in a pixel-to-pixel resistance of 1 GΩ. As shown in figure 4.5 the center is divided in four so-called "bulls-eye" pixel which are surrounded by twelve concentric rings, each consisting of 12 pixels. Since every pixel covers the same area the radii of the rings get smaller to the outside. Additionally each ring is shifted against their adjoining rings by 15 degrees. This design allows the wafer to cover a flux of about 210 Tcm^2 in a magnetic field of 3.3 T. (All numbers and data are taken from [62]).

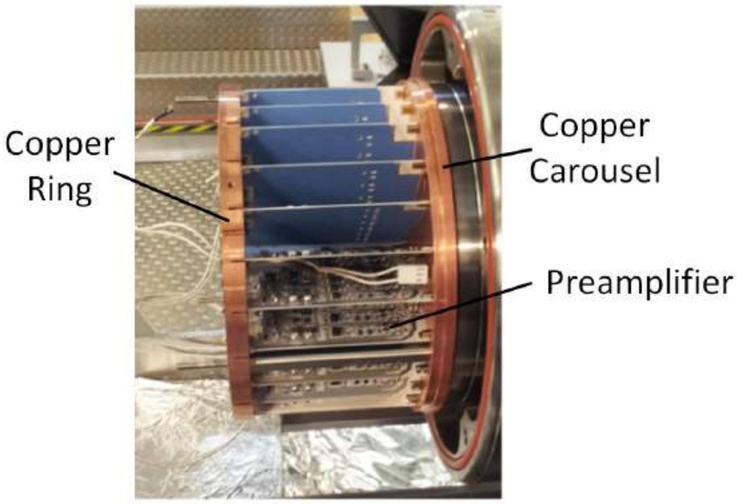

Figure 4.4: Pre-amplifiers are cooled with the heat pipe. In order to efficiently transfer the heat the pre-amplifiers are embedded into a copper carousel (copper plate with holes for feedthrough pins) and a copper hold-down ring on the the other side. Additionally they are enclosed by a copper mantle which is not shown in the picture.

The presence of leakage currents and its influence on the detector wafer performance requires improvement. Leakage currents, typically below 1 nA per pixel, exist due to a tiny but subsisting amount of free charge carriers in the intrinsic layer leading to a low electrical conductivity. Overlapping with the signal of source electrons the leakage current worsens the energy resolution of the detector wafer. To counter this effect several methods to reduce the leakage current are possible: Firstly, a broader intrinsic layer increases its electrical resistance. Secondly, cooling the detector material reduces thermal excitations. And lastly, applying a reverse bias voltage increases the thickness of the depletion zone in the PIN-diode and thus the number of free charge carries within [55]. To bias the detector wafer with nominal voltage of $U_{\mathrm{bias}} = 120\,\mathrm{V}$ the front side of the wafer is coated with a non-oxidizing TiN [66, 50]. This coating reaching over the edges (bias ring in figure 4.5) allows to apply voltage from the segmented backside. Further the TiN coating assures low-background and low-radioactivity properties [66, 67]. The bias ring influences the performance of the outer pixels due to field distortions originating from the applied voltage, which is minimized by a 2 mm broad guard ring between the bias ring and pixels [62].
The wafer is mounted on a custom made feedthrough flange, shown in figure 4.6. Establishing the electrical connection for the signal readout spring loaded and gold-plated pogo pin connections press with a force of 50 N onto the segmented backside of the wafer. This causes a slight deformation of the wafer of 0.24 mm which has no influence on the detector performance [66].

Since the SDS-I wafer has shorted pixels a visual investigation of the segmented wafer backside was made to reassure it is not a connection problem of the pogo pins. Therefore the insulating boarders between the pixels were examined with a light microscope in a clean room. The images in figure 4.7 show parts of the wafer backside: The pixels itself are displayed in yellow, the insulating boarders in blue. Results show a damaged insulating pixel boarder on the SDS-I wafer [68], shown in the left. The image on the right shows a partly damaged insulating boarder of pixels

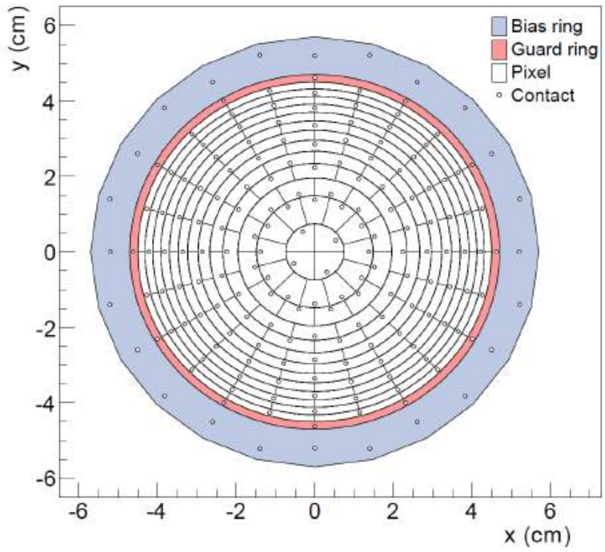

Figure 4.5: Segmented backside of the detector wafer. Surrounding the 148 pixel is a guard ring (red) and a bias ring (blue).Figure adapted from [**?**].

on the test wafer. More impurities found on the wafer are in shown in [69, 70]. To what extend these impurities influence the detector performance is unknown.

4.6 Readout Electronics and Data Acquisition

Electrons which impinge on the detector wafer induce a charge signal which is collected on the p-doped backside of the wafer. This signal goes through the pogo pins and is picked up on the other side of the feedthrough flange by charge-sensitive preamplifiers. These are mounted in groups of 6 or seven on 24 circularly arranged modules which cover all 148 detector pixels (shown in figure 4.8, top left). The amplified signals of these modules are carried on by two circular distribution boards and a cable harness, shown in figure 4.8 (top right) which also distribute the detector voltage of up to +120 V. At the end of the HVac chamber a second feedthrough flange transfers the signals to the ambient air electronics (shown in figure 4.8, bottom left) located in a Faraday cage. The Faraday cage houses four optical sender boards (OSBs), a temperature monitoring card and a Power and Control (PAC) board (figure 4.8, bottom right). Variable gain-stages on the OSBs allow to amplify the analog detector signals and execute the energy calibration pixel wise. The temperature monitoring card, reading out all temperature sensors along the PAE, can only be plugged in temporarily as long as no voltage is applied to the PAE. The PAC board supplies power to the vacuum electronics and OSBs and further contains temperature readouts for vacuum electronics, power-conditioning circuits, over-voltage protection as well as variable-gain control and monitoring for digital-to-analog converters on the OSBs in order to run the electronics as well as set their parameters. Further it is able to read out the leakage current of single pixels, the temperature of individual preamplifier modules as well as applying the reverse bias voltage to the detector wafer. All parts of the read-out chain described up to now are at post-acceleration potential while the data acquisition system (DAQ) is grounded. Therefore, the detector signals are converted from analog to optical on the OSBs and are sent via optical fibers to the DAQ where thy are transformed back before being digitized. The DAQ itself consists

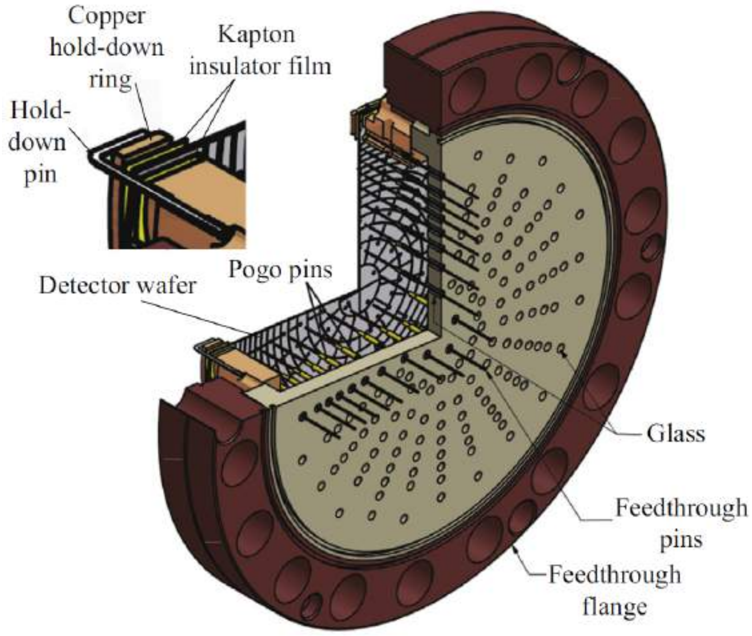

Figure 4.6: CAD drawing of the detector feedthrough flange. Spring-loaded pogo pins press against the wafer which is held in place by a copper hold down ring and L-shaped hold-down pins. Figure adapted from [**?**].

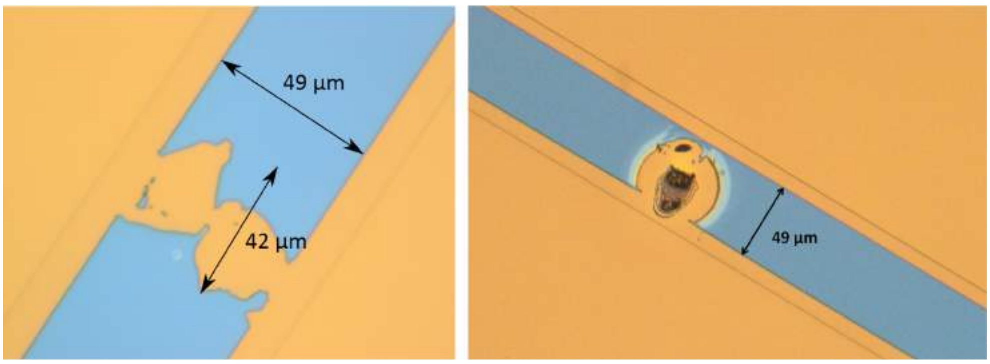

Figure 4.7: Enlarged view of wafer backside images the boarders between pixels via an optical microscope. This visual inspection showed impurities occurring on the inspected wafers. Figure (a) shows the SDS-I wafer where two pixels are shorted (#67 and #68) [68]. Figure (b) shows that the insulation between two pixels on the test wafer is damaged but not fully shorted [69].

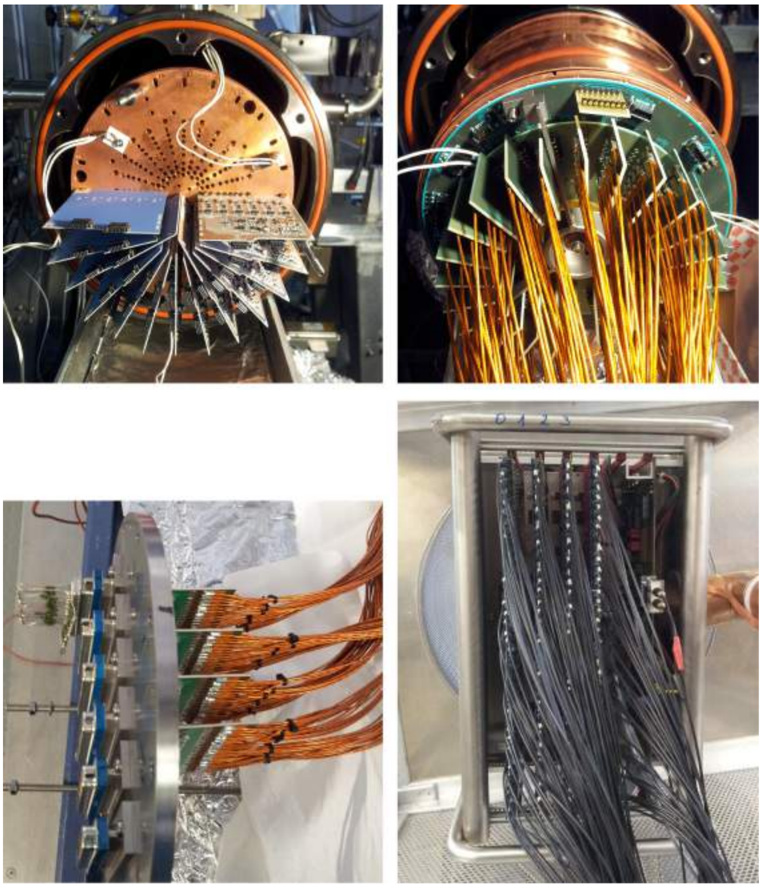

Figure 4.8: The read-out electronics chain of the FPD starts with the pre-amplifiers modules, shown halfway installed in the top left figure, which pick up the signals from the wafer. Afterwards the signals are fed by the cable harness, which connects to the distribution board shown in the top right figure, to the ambient-air feedthrough flange (bottom left) where the harness sockets into sub-D connectors. On the ambient air side optical sender boards (bottom right) lead the signals to the data-acquisition system.

out of eight first-level trigger (FLT) cards and a secondary-level trigger (SLT) card. The FLTs determine the energy and time of each event with high precision using a trapezoidal filter. This filter uses two parameters shaping length L and the gap length G, both changeable by ORCA. While the shaping length averages out the noise in the data the gap length assures that the signal peak (200 ns rise time and a fall time of 1 ms) is excluded when averaging out the noise [71, 62]. All FLTs are coordinated, initialized and synchronized by the SLT card which transfers the signal to the DAQ computer where the data is processed by a software package called ORCA and is stored in form of root files in the KATRIN database [55].

4.7 Calibration Sources

To calibrate the FPD different calibration sources are installed in the system, e.g. a test-pulse injection to the vacuum electronics and a γ-source. Data taken for this thesis has been calibrated with the ^{241}Am γ-source, which is why only this source will be described in the following.
The γ-source can be moved in and out of the beamline remotely via a system of pneumatic driven motors and bellows without disturbing the UHVac. As shown in

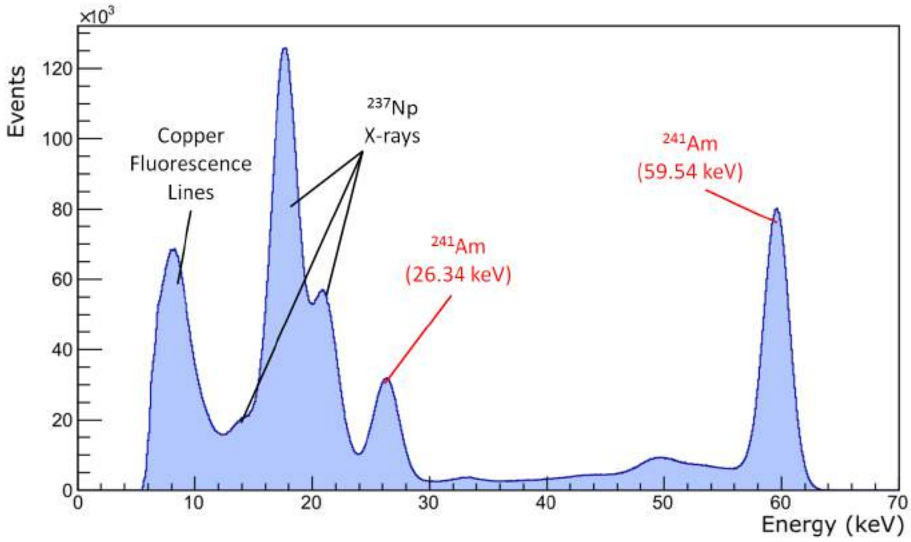

Figure 4.9: The global ^{241}Am spectrum, here measured with the SDS-I wafer, shows several different peaks. To calibrate the detector the mono-energetic γ-lines at 26.34 keV and 59.54 keV are used. In addition there are a copper fluorescence lines and several X-ray lines originating from the excited daughter nuclei ^{237}Np. Spectrum taken with SDS-IIb wafer

figure 4.9 the global spectrum of ^{241}Am measured by the detector has characteristic mono-energetic γ-lines at 26.34 keV and 59.54 keV. These γ lines are used to calibrate the detector ADC spectra pixel wise in the keV range. Together with the zero point in these separate spectra a calibration can be determined and applied through a linear fit according to $\mathrm{E} = m \cdot \mathrm{ADC} + \mathrm{c}$. The width of the lines gives the energy resolution of the detector as described in chapter 6.2. Additional fluorescence lines originate from the copper PAE and X-ray lines from exited ^{237}Np*, the daughter nuclei of ^{241}Am are usually not used in the detector calibration but allows to investigate the linearity of the detector electronics [55]

4.8 The Veto System

To reduce the impact of background events to the data the detector wafer is surrounded by a veto system. The veto triggers to passing cosmic muons and allows to exclude coincident detector events.
The current veto has been recently build and installed into the FPD system. It consists of eight panels and two end cap parts. The panels are installed within the warm bore of the detector magnet outside of the lead shielding. Within each panel two wave-length shifting WLS optical fibers are used to avoid photon loss. These fibers allow to determine where exactly muons passed through the panel and, thus, if they will induce a signal on the detector wafer. Read-out electronics are compatible to work in a magnetic field and are attached below the DET magnet. They run with a custom made software which is currently tested and improved.
The advantage of this new system compared to the previous system, described in [62, 72], is that it does not require cooling and the fibers inside the panels are easily replaceable if damaged. Furthermore it can be fully computer controlled, has an automatic temperature compensation and an embedded calibration.

5. High Voltage Tests of the Post-Acceleration-Electrode of the FPD system

The Post-Acceleration-Electrode (PAE) housed in the FPD system is used to accelerate signal electrons which pass the MS MAC-E filter to boost their energy to regions of low intrinsic detector background. As described in section 4.2 it is a trumpet shaped full copper electrode which is put on positive voltage. Being designed to operate at voltages up to +30 kV it faces breakdowns when exceeding +11 kV. These breakdowns pose a danger to the sensitive and expensive electronics of the FPD such as the pre-amplifiers. In order to further study the breakdown behavior of the PAE without risking damage to the detector electronics a standalone PAE test stand was assembled by KATRIN collaboration partners at the University of Washington (UW) using spare components of the FPD. The discharge phenomena which are likely to occur at the FPD or the test stand are described in section 5.1. The setup in section 5.2. The performed high voltage tests as well as the observations made are discussed in section 5.3 before conclusions for the FPD system at KIT are drawn in section 5.4.

5.1 Discharge Phenomena

High voltages (HV) poses a risk to oneself as well as to used electronics if not grounded properly. Unfortunately, HV and the variety of discharges or breakdown phenomenons are not yet fully understood in detail. The following subsections give a short glimpse on the breakdown phenomenon concerning the KATRIN experiment as well as the test stand built at UW. Most important are hereby the field emission, the Paschen law and the Penning traps. Countermeasures for the latter have already been developed and installed at KATRIN.

5.1.1 Field Emission

Field emission (FE) describes the emission of electrons from a surface due to the presence of an electrostatic field. The potential barrier an electron experiences within a metal surface is deformed by this electrostatic field and, thus, leads to a significant higher probability for electron to overcome this barrier (Fowler-Nordheim tunneling [73]). This occurs to any weakly or non-conducting dielectric (such as gases, solids or vacuum) in high electric fields. FE is seen as the primary source for electrical or vacuum breakdown [74], but is also used for specific applications such as high resolution electron microscopes [75]. In the following two significant discharge mechanisms are described.

Townsend Mechanism
In high vacuum the discharge is described by the Townsend mechanism: An electron, which has overcome the potential barrier, is accelerated by the applied electric field. If the mean free path of the electron is long enough it is able to gain enough energy before colliding with residual atoms which it then ionizes creating secondary electrons (SE) and ions. The required voltage for this process depends on the residual gas. These SE are also accelerated by the potential of the electric field and cause further ionization (avalanche effect). Discharges based on the Townsend mechanism are self sustaining if the power supply keeps providing current [76].

Vacuum breakdown
A vacuum breakdown is initiated by field emission from microprotrusions on an electrode surface within a good vacuum and no magnetic field. Microprotrusions are small tips at which the electric field is enhanced. A higher field can induce local heating which leads to melting of the surface in this particular spot building metal vapor which then locally degrades the vacuum and can result in gaseous breakdown with ionization. This shows how important it is for a system to have smooth surfaces when operating with HV in order to avoid breakdowns. Smoothening the surface can be achieved by electro- or mechanical polishing as well as via ion bombardment. Vacuum breakdowns are a surface dominated phenomenon depending on the properties of the used material, thus, residual gases as well as the presence of a magnetic field have an minor influence [76]. The breakdown is a voltage dependent phenomenon described by the Paschen Law for a certain vacuum pressure regime (see section 5.1.2).

Triple Junctions
Triple junctions are an intersection of a metallic surface with a dielectric surface located within a vacuum. It can cause field enhancements initiating a discharge (via surface avalanche effects) already in relatively low electric fields. In high voltage systems the insulators surfaces are the weakest components because they are a good source of ionizable material and discharges preferably propagate along surfaces. Further field enhancements fostering discharges may be caused via charged insulator surfaces from previous discharges, since the charge is not able to redistribute itself due to its non-conducting properties. Triple junctions are not yet fully understood nor described but show a notable influence when operating with HV.

5.1.2 Paschen Law

The Paschen law describes the breakdown voltage between electrodes as a function of vacuum pressure and gap length. The equation was empirically discovered in 1889 [77]:

$$\mathrm{V} = \frac{\mathrm{B} \cdot \mathrm{p} \cdot \mathrm{d}}{\ln\left(\mathrm{A} \cdot \mathrm{p} \cdot \mathrm{d}\right) - \ln\left(\ln\left(1 + \gamma_{\mathrm{se}}^{-1}\right)\right)} \tag{5.1}$$

Deriving this equation shows the associated Paschen curve has a minimum, illustrated in figure 5.1. For small p·d (left side of the minimum) the electrons gain enough energy to ionize atoms, however, their mean free path is very large and so it becomes

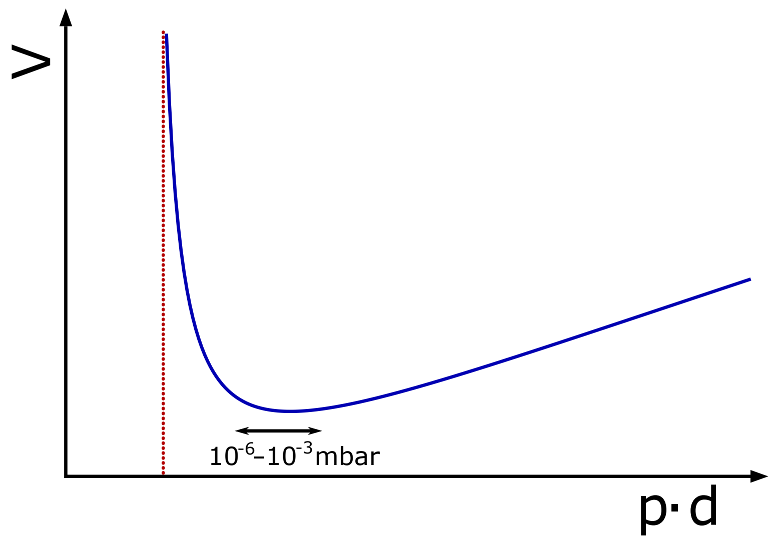

Figure 5.1: The Paschen curve illustrated, shows schematically the breakdown voltage as a function of pressure and electrode distance p·d. The exact position of the minimum depends the residual gas and the material of used electrodes in the vacuum system. For low pressures the number of gas atoms is low and, thus, the probability of a collision is low resulting in less ionization. At higher pressures the mean free path of the electron is too short to obtain enough energy for ionizing other atoms. Figure adapted from [78].

more likely for these electrons to reach an electrode rather than ionize an atom. This results in an increase of the breakdown voltage. On the other side of the minimum, a higher gas pressure results in a shorter mean free path for the electrons. With a higher probability of collisions the electrons are unable to gain enough energy in order to ionize atoms. Further, with each collision the electron trajectory is forced to change the direction. Therefore, the breakdown voltage increases for higher p·d. However, the exact course of the function as well as the position of the minimum depends on the gas type as well as the electrode material.

5.1.3 Penning Traps

Penning traps arise when an electric and magnetic field are in a specified configuration. As illustrated in figure 5.2 the electromagnetic field creates a localized volume in which charged particles are stored. For example, a low-energy electron generated in a potential U_0 is trapped in between two cathodes with $U < U_0$ in axial direction. A perpendicular motion is suppressed by the of the magnetic field induced Lorentz force which drives the electron back to its starting position. After a period of time the stored particles gain enough energy to ionize residual gas, resulting in secondary electrons as well as ion or photons. Ions and photons are able to leave the trap and thus create additional background in the spectrometer [79, 80]. Another aspect is that the penning trap is filled by a large number of additional (secondary and tertiary) electrons which can generate an unstable plasma which causes a penning discharge [81, 82]. Next to creating large background in the spectrometer the discharges pose a risk to the experimental apparatus [83]. In order to avoid harmful and background generating discharges specific custom made, so-called penning wipers have been developed and installed.

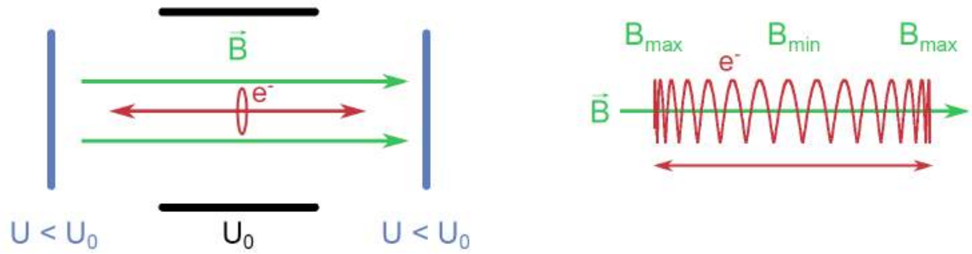

Figure 5.2: The Penning trap is created with the electric and magnetic field in a certain arrangement forcing the electron to remain within a specific region. On the left side the electron is trapped horizontally between two electrodes and the perpendicular motion is suppressed by the Lorentz force induced by the magnetic field. This forces the electron to do a cyclotron motion around magnetic field lines. On the left side is shown, that the electron can solely be trapped by an inhomogeneous magnetic field (magnetic mirror effect). Figure adapted from [80].

5.2 The Test Apparatus

To set up the PAE test apparatus old parts of the FPD system were used. An old PAE and spare quartz tubes with foil electrodes on their surfaces were shipped to UW. In comparison to the setup at KATRIN, this apparatus has been modified in order to visually observe the breakdown effects as shown in figure 5.3.
The custom made blanking plate, closing the vacuum chamber on the upstream end of the PAE, is equipped with a high voltage (HV) feedthrough and a small pump port, shown on the left in figure 5.4. However, the welding quality of the used metal was very poor which caused difficulties reaching the desired vacuum quality in the chamber. An adequate sealant was not able to close the leak such that temporarily a putty of modeling clay was used instead. This lead to sufficient but not good vacuum. An observation window made out of acrylic glass is displayed on the right in figure 5.4 which shows a view in upstream direction. Further in this figure the custom made extension of the vacuum chamber is shown which allows to use the big and medium quartz tube within the apparatus. In order to be able to insert the medium quartz without damaging the ground connector of the outer electrode a groove had to be filed into the extension as shown in figure 5.5. To apply high voltage to the PAE a Spellman power supply which provides up to +30 kV was used. For all measurements a Pirani gauge was mostly operated at its extreme lower range (lower 10^{-3} torr) which is why all given pressures should be handled with care.

Except the initial tests described in section 5.3.1 all tests have been executed with the following procedure: every five minutes the voltage was increased by +1 kV while starting measurements after reaching +10 kV. This procedure is referred to as "slow ramp test".

5.3 High Voltage Tests

5.3.1 Initial Tests

Prior to executing controlled HV tests an initial conditioning of the PAE was conducted while ramping the voltage in exploratory fashion. Since the used parts were exposed for a very long time first conditioning effects could already be observed at 5 kV with a pressure of $3.7{\cdot}10^{-3}$ torr. In several ramps of voltage the maximum

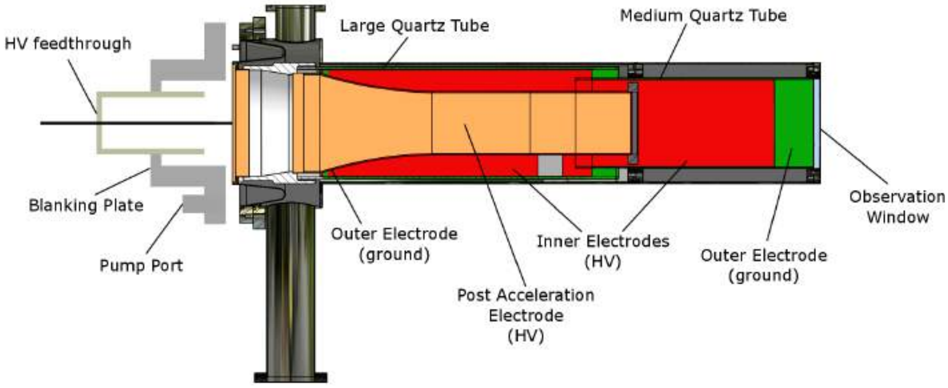

Figure 5.3: The modified apparatus has a custom made blanking plate on the upstream end and an acrylic observation window on the downstream end of the PAE. Further the position of the quartz tubes and their foil electrodes are displayed.

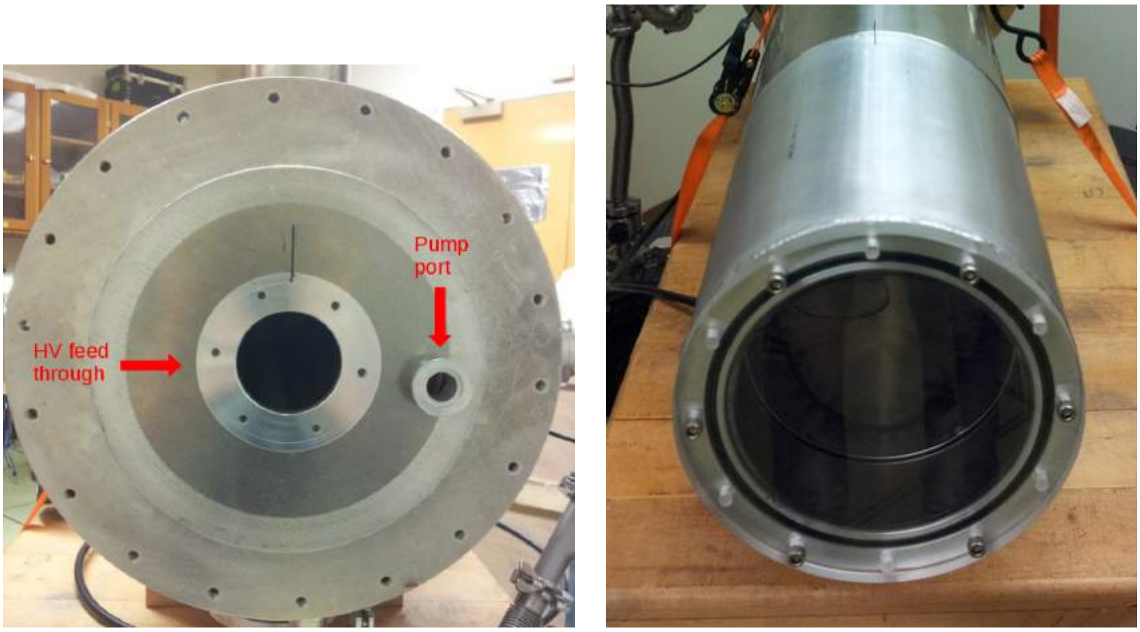

Figure 5.4: To the right the custom made blanking plate with a HV feedthrough and a pump port is shown. The acrylic observation window attached to a custom made extension is shown on the right side.

Figure 5.5: In order to be able to insert the medium quartz tube into the system a groove had to be filed into the custom made extension chamber. In the left figure the ground connector of the outer electrode does not fit into the extension. The figure to the right shows the groove which was filed in allowing to insert the quartz tube with its ground connector.

achievable voltage without a continuous breakdown was increased which indicates a more and more conditioned system. Maximum achieved voltage was +27 kV after the freshly conditioned system pumped over night and reached a pressure of $2.4{\cdot}10^{-3}$ torr. Observable effects were: 1) Flashes from various regions within the chamber which were mostly accompanied by a tinny noise originating from the upstream end of the PAE. 2) As expected the pressure rose during breakdowns. 3) The medium quartz tube was occasionally partly or fully glowing and 4) while ramping the voltage the quartz tube lit up at several spots probably due to charge redistributing itself.

5.3.2 Pressure Dependent Tests

Before continuing voltage tests the system was vented to air to mount a venting valve for controlled gas inflow and an ion gauge. The ion gauge turned out not to be useful due to the high pressure in the chamber which exceeded its measurement range. The lowest achieve pressure of $2.5{\cdot}10^{-3}$ torr. In order to make first observations several slow ramp tests were executed at different pressures:

- $2.5{\cdot}10^{-3}$ torr: first breakdowns occurred at +14 kV, becoming more frequent when exceeding +17 kV. Further the medium quartz tube was occasionally again partly or fully glowing. At +25 kV a continuous breakdown started. Flashes mostly occurred around the PAE blanking flange ($\hat{=}$ feedthrough flange in FPD system).
- $5.1{\cdot}10^{-3}$ torr: Similar observations as at $2.5{\cdot}10^{-3}$ torr, but with continuous breakdown starting at +15.5 kV.
- $1.3{\cdot}10^{-2}$ torr: Already at +2 kV continuous breakdowns occurred with glow discharges.

The achievable pressure lies probably close to the region of the Paschen minimum, far from the desired vacuum pressure as it is at the FPD system.
Nevertheless, these tests showed roughly where within the PAE chamber the discharges occur and at what pressures the dominant discharge effect changes. Despite the vacuum further tests were carried out in order to gain a better understanding of the locations where the breakdowns are initiated most often.

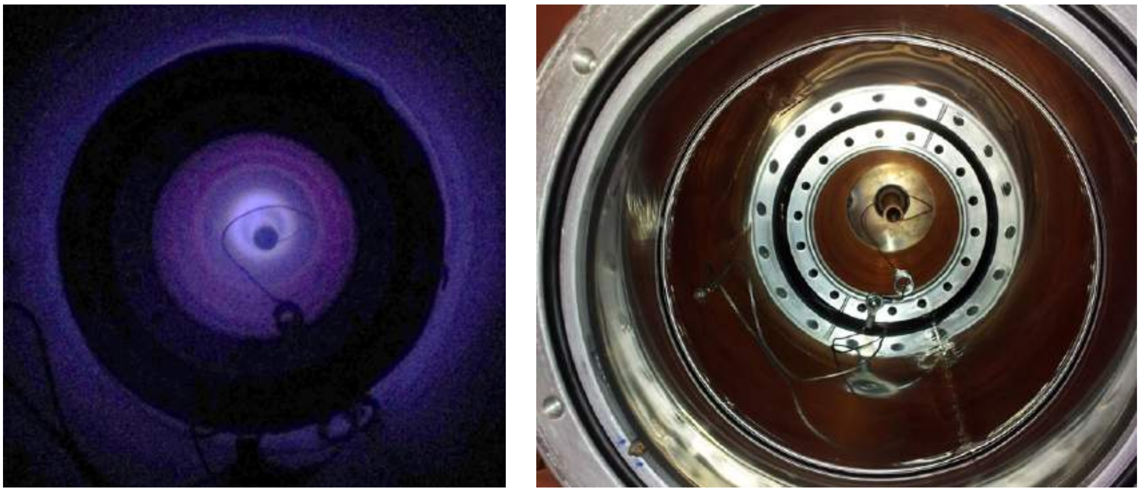

Figure 5.6: View through the observation window with the PAE flange taken off. Right: The blanking plate with the HV feedthrough can be identified at the far end of the PAE. Left: Glow discharge emanating from the blanking plate.

5.3.3 Modified System - Improvement of Sight

To extend the sight within the chamber the PAE flange was taken off, enabling a direct view on the blanking plate at the far end of the PAE (right side of figure 5.6). During a slow ramp test the following observations have been made: 1) the blanking plate surrounding the HV feedthrough was glowing bright like in a glow discharge, shown on the left side in figure 5.6. 2) Flashes within the PAE at the far end (exact position could not be localized due to restricted field of view). The decision was made to use the phenomenon of the glow discharge at the blanking plate as the principal means to clean and condition the system.
Thus the voltage was ramped up again, until the glow discharge commenced at 27 kV. The voltage dropped to 4.5 kV while the current increased to 0.75 mA and the pressure to $8.9{\cdot}10^{-3}$ torr. After maintaining the system in this state for nearly three hours the voltage had increased to 8.5 kV while the current remained the same and the pressure decreased to $6.3{\cdot}10^{-3}$ torr.
The first slow ramp test after this long-term conditioning showed no more continuous breakdowns up to +30 kV. However, occasional breakdowns were observed for voltages >+14 kV. The pressure slowly rose with increasing voltage to $2.9{\cdot}10^{-3}$ torr at +30 kV.

5.3.4 Influence of Gas-Exposure on Conditioning

With the system conditioned the effect of an exposure to different gas species on the HV stability was investigated. First the system was vented with air to atmospheric pressure and pumped out again after 15 h of exposure. Already during pump down a loss of conditioning was indicated since it took 78 hours to come down to the lower 10^{-3} torr regime. This is attributed to water vapor sticking to the walls or being trapped between electrode foils and the quartz. A subsequent slow ramp test supported this assumption: Breakdown behavior as prior to the conditioning started at 15 kV. A pulsating glow within the medium quartz tube was observed which sometimes increased in intensity resulting in a breakdown but mostly fades away over a short period of time.
In a next step the system was exposed for 17 hours to argon at atmospheric pressure.

After pumping for 2 hours the pressure reached $2.6{\cdot}10^{-3}$ torr again. A slow ramp test showed again the previously observed breakdown behavior: First breakdowns at +17 kV followed by a more frequent appearance when exceeding 22 kV. Even when exposing the system for a short period time, e.g. during quick modifications at the vacuum system a loss of conditioning could be observed.

5.3.5 Observations - Summarized

Several different phenomena were observed during HV breakdowns of the PAE:

- When significant breakdowns occur the pressure may rise by up to an order of magnitude.
- At moderate voltages (<20 kV) flashes mainly occurred behind the PAE flange (determined through bolt holes of this flange). At higher voltages (>20 kV) flashes also appeared close to the observation window.
- Nearly all of the flashes are accompanied by a tinny noise originating from the far end of the system (around PAE ceramic).
- The medium quartz tube occasionally began to glow party or fully. This could be due to fluorescence of the quartz glass or when it functions as a light conductor. This glow lasted between a few seconds and a couple of minutes. In addition a pulsating glow was observed which tended to fade away over time, but occasionally increased in intensity and resulted in a discharge.
- Massive discharges were accompanied by the HV cable lighting up over a length of up to 50 cm. This could cause damage to any electronics which are connected to or touching the cable. Further these discharges produce RF noise which can be picked up by cables or other parts of electric devices functioning as antenna and in this way harm electronics or generate noise in the detector signals. E.g. during the tests the sensitive input FET of the ion gauge controller was destroyed twice, and the more robust Pirani gauge readout displayed a "fault" error frequently after discharges.
- Small lit up spots were observed during ramping the voltage up or down. This could be due to charge accumulation on the insulator surface (quartz) before it redistributes itself.
- Glow discharges that emanate from the blanking plate could be observed and were utilized to condition the system. This process removes residual contaminations such as water vapor, oxygen or residuals of the sealant adhering to the chamber walls. After conditioning no more continuous glow discharges were observed at pressures of $\sim 10^{-3}$ Torr and for voltages up to +30 kV.
- The observation window was bombarded by ions emitted by the glow discharge at the blanking plate. Since the window acts as an insulator the charge accumulated which leads to surface discharges towards the metallic extension chamber, there, causing a bright flash.

When dismantling the system the used sealant was found not to be cured. This probably induced a vapor pressure explaining the rather poor vacuum quality of the system. In addition, sharp edges, which are known to enhance electric fields, were

Figure 5.7: The left figure shows that notches have been cut out of the outer electrode foil on the medium quartz tube. The notches are located in a high field region according to [84]. The right figure shows where the sealant penetrated into the vacuum chamber can be seen.

Figure 5.8: The stainless steel support saddle is supporting the big quartz tube. Right: design of the saddle and supposed position within the vacuum chamber. Left: the inner electrode of the big quartz tube has a direct line-of-sight onto the grounded saddle.

found within high field regions according to [84] on the outer electrode of the quartz tubes, especially at the medium one. As shown in figure 5.7 part of the electrode has been cut out. Another potential reason for the HV breakdowns could be the direct line-of-sight. Surface discharges exist and tend to go to components which are at a different electric potential such as the grounded stainless steel support saddle. Figure 5.8 shows the latter in the intended position.

5.4 Conclusion

Further studies at lower pressures are required to fully understand the PAE breakdowns above 10 kV. However the following conclusions can be drawn from the first series of test measurements at poor vacuum:

- A power supply which does not trip off during continuous breakdowns is required for effective conditioning.
- The most effective conditioning is achieved by initiating a glow discharge at a pressure of $\sim 10^{-2}$ Torr. This discharge should be continued until the pressure and current read-back begin to fall.

- HV breakdowns of the PAE can harm the sensitive electronics. No attempt should be made to condition the PAE when the pre-amplifiers are installed. It is quite possible that equipment like pressure gauges, RGA's, Pulcinella electronics, and equipment associated with the magnets etc. could be damaged.
- After long-term conditioning, even though voltages of +30 kV were achieved without continuous breakdown, intermittent breakdowns occurred every few minutes. These would probably pose a risk the electronics as well.
- Despite the limited visibility it appears that most of the sparks come from the region just behind the PAE flange, and to some extent from the far end of the PAE where the large quartz tube sockets into the insulator ring. Both are regions where high fields, as identified in [84], and triple junctions exist.

For upcoming measurements with the PAE test stand at UW a new, leak free blanking plate should be build in order to operate the system under realistic vacuum conditions which are similar to the FPD system. Furthermore, the breakdowns should be investigated as a function of foil-electrode position on the quartz tube. For reproducibility reasons and ease of operation the ramping of voltage should be automated. An automated way of recording breakdowns as a function of time, in combination with a camera looking through the window would be a powerful improvement of the system in terms of data taking.

6. Commissioning and Characterization of the Detector

In 2016 the FPD system was operated with two different wafers were installed and run in : a test wafer and the later SDS-IIb wafer. For the detector calibration the ^{241}Am source was used as described in section 4.7. In this chapter the performance tests of the different wafers are described which were carried out with the FPD system in a separated stand-alone mode where it was mechanically disconnected from the main spectrometer. Section 6.1 details the spatial resolution of the wafers, whereas section 6.2 concentrates on the temperature dependency of their mean energy resolution. The intrinsic detector background rate for the two different wafers as a function of the applied PAE voltage is analyzed in 6.3.

6.1 Spatial Resolution

The installed detector electronics allows to read out each pixel separately and, thus, a single-pixel energy resolution can be derived. A figurative representation of these single-pixel energy resolutions in the schematic shape of the wafer backside enables to visualize the spatial distribution of the per-pixel resolutions across the wafer. The energy resolution of the individual pixels is calculated with the full width half maximum (FWHM) method by analyzing the 59.54 keV peak of the ^{241}Am spectrum.

Figure 6.1 shows the distribution of the energy resolutions across the SDS-I wafer (shorted pixels #78 and #89 were excluded from the analysis). The energy resolutions are not randomly distributed across the wafer showing a decrease towards the top half of the wafer. Figure 6.2 shows the distribution across the SDS-IIb wafer improving towards the inner pixels rings. The origin of this phenomenon is not yet clear. A possible explanation are the different noise contributions for each pixel. Another possible explanation may originate from custom made feedthrough which guides the signals from the preamplifiers to the ambient air electronics. Tolerances of these front-end electrics lead to a different performance for individual channels [55]. The right side of figure 6.2 shows the distribution of the energy resolutions a mean of 2.3 keV. In comparison, for the SDS-I wafer the mean energy resolution was 1.5 keV [55]. The different performance may originate from the fact that the SDS-I and SDS-IIb wafer are from different batches. However, a reinstallation of the SDS-IIb wafer at a later point showed similar characteristics regarding the spacial resolution, but a worsened mean energy resolution of 2.6 keV, see figure 6.4. Note that this

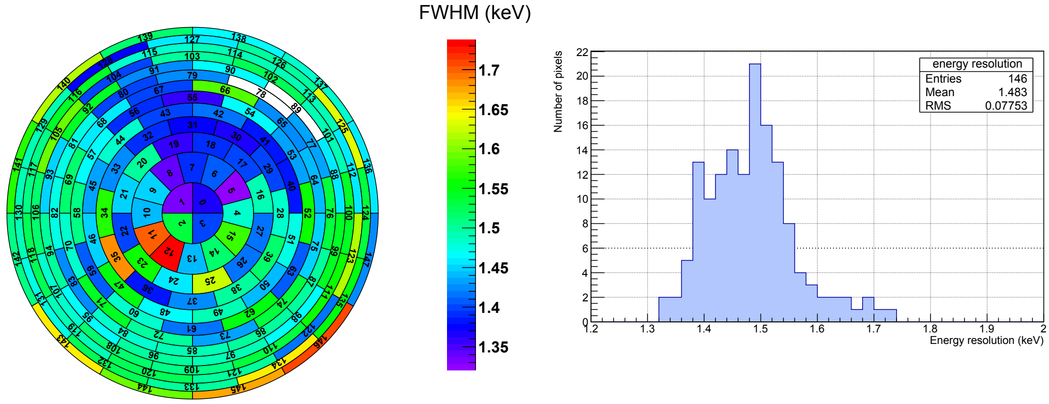

Figure 6.1: Energy resolution of individual detector pixels during the SDS-I measurement phase. Two pixels are shorted (#78 and #89) and therefore taken out of the analysis. The energy resolution (FWHM) is derived through a Gaussian fit of the 59.54 keV peak of the ^{241}Am source (runs #4005 - #4036). Left: Individual energy resolutions of the pixels are not randomly spread across the wafer. The pixels in the top half of the detector wafer show a decreasing energy resolution . Right: Distribution of energy resolution of pixels around a mean value of 1.5 keV (FWHM).

wafer has been kept mounted on the feedthrough flange and stored in a nitrogen atmosphere in the mean time. Investigations at the FPD system to identify a reason for a different performance show no clear origin and are still in progress. Since this wafer has been in use its energy resolution gradually becomes worse over time, however, the cause is yet unknown. Between the end of the SDS-II and the beginning of the SDS-III measurement campaign another detector wafer was installed into the FPD system as a test. The performance of this wafer is shown in figure 6.3. It, too, shows a slight tendency in its spatial distribution of energy resolutions improving towards the center. However, the inferior mean energy resolution of 2.9 keV turned out to be unsatisfying and, thus, the SDS-IIb wafer was installed for the SDS-III measurement campaign.

6.2 Energy resolution

The mean energy resolution of a wafer, derived by a Gaussian fit of the distribution of resolutions per pixel, is influenced by the temperature of the detector wafer and the front-end electronics. This can be explained by a lower thermal noise in the wafer [65]. To investigate the change in energy resolution as a function of the temperature, measurements with the Am-source were performed during cool-down of the FPD system (the runs that are analyzed are listed in table 6.1 and 6.2). One data point equals one hour of data taking time. For analysis the read-out of the temperature sensor on the copper carousel (T_{carousel}), shown on the upper left in figure 4.8, is used.

Figure 6.5 shows the data from the cool-down with both the SDS-IIb wafer (circular data points) and the test wafer (triangular data points) reinstalled (runs #27624 - #27712). As the temperature decreases the energy resolution decreasing accordingly, as expected. Furthermore, at lower temperatures the leakage current becomes smaller, as described in 4.4. A linear fit shown in red for the SDS-IIb wafer derives a change

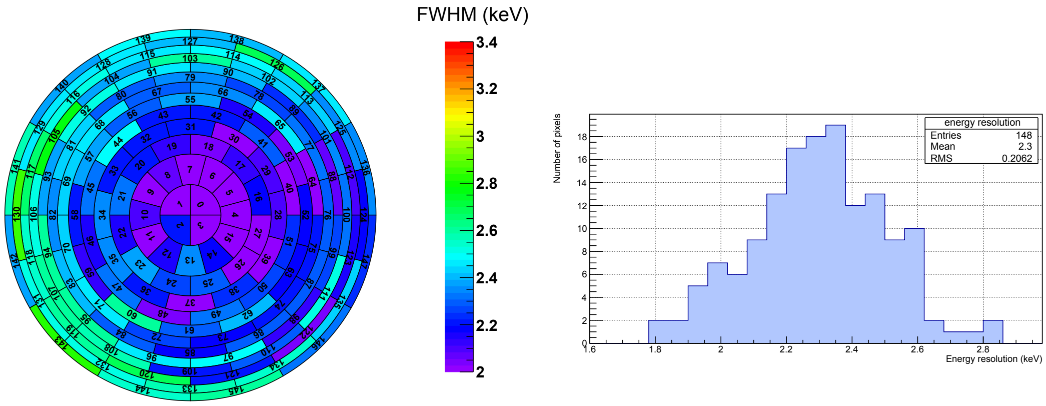

Figure 6.2: Energy resolution of individual detector pixels during the SDS-IIb measurement phase. The energy resolution (FWHM) is derived through a Gaussian fit of the 59.54 keV peak of the ^{241}Am source (runs #23082 - #23085). Left: Individual energy resolutions of the pixels are not randomly spread across the wafer, but are decreasing towards the inner pixel rings. Right: Distribution of energy resolution of pixels around a mean value of 2.3 keV (FWHM).

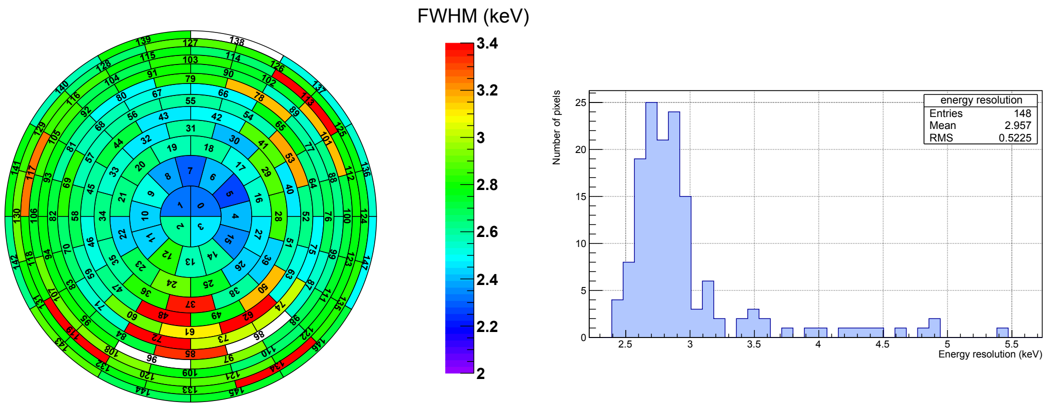

Figure 6.3: Energy resolution of individual detector pixels with a test wafer installed. The energy resolution (FWHM) is derived through a Gaussian fit of the 59.54 keV peak of the ^{241}Am source (runs #27134 - #27149). Left: Like as the SDS-I and SDS-IIb wafer this one, too, shows a radial dependency with an increasing energy resolution towards the outer pixel rings. Right: The mean energy resolution of ∼3 keV (FWHM) is worse compared to the SDS-IIb wafer.

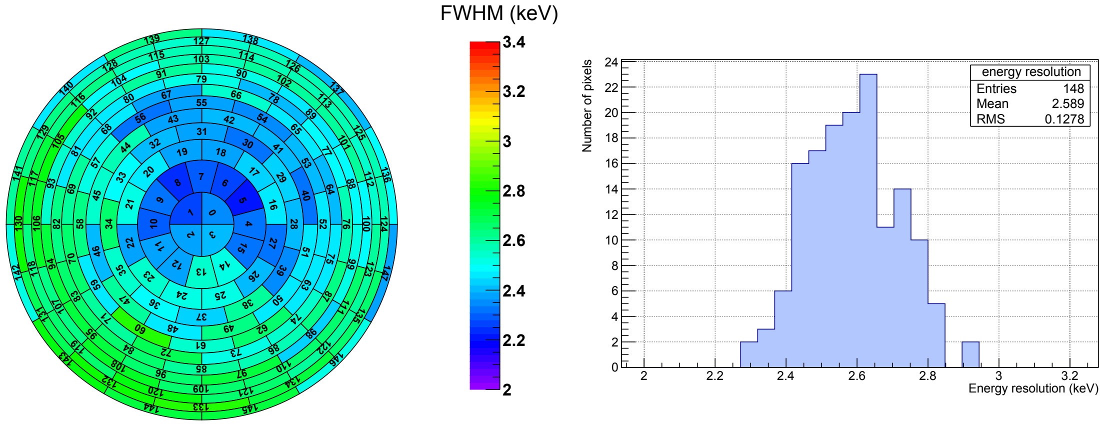

Figure 6.4: Energy resolution of individual detector pixels for the reinstalled SDS-IIb wafer. The energy resolution (FWHM) is derived through a Gaussian fit of the 59.54 keV peak of the ^{241}Am source (runs #27539-#27555). Left: The SDS-IIb wafer still shows an increase of the energy resolution towards the outer pixel rings. Right: Distribution of energy resolutions per pixel around a mean value of 2.6 keV (FWHM).

in energy resolution of $P_1 = 5.0\,{}^{\mathrm{eV}}/_{\circ\mathrm{C}}$. Extrapolating this to lower temperature better energy resolutions are achievable. However, this linearity only applies to a certain temperature regime, at higher temperatures the energy resolution decreases exponentially and at lower temperatures it reaches a constant plateau [55]. In the measurements with the SDS-IIb wafer the lowest achieved temperature of the FPD system was -20°C. However, in the past the system has shown to be able to reach lower temperatures, e.g. -40°C with the previously installed test wafer. Even at these lower temperatures the mean resolution of the test wafer (runs #26920 - #27031) turned out to be still inferior to the SDS-IIb wafers. A linear fit, shown in blue in this figure, derives a change in energy resolution of $P_1 = 4.4\,{}^{\mathrm{eV}}/_{\circ\mathrm{C}}$. The smaller value of P_1 for the test wafer may originate from a different noise behavior of the read out electronics. However, the same electronics are used for both wafers except the feedthrough flange with its spring loaded pogo pins inducing different pressures on individual pixels which may influence the performance of the wafer differently from the flange on which the SDS-IIb wafer is mounted on. Furthermore, different wafers may have different noise sources dominating on the individual wafer.

6.3 Background Measurements

The FPD system relies on a low intrinsic background to measure incoming electrons from the MS with high signal-to-noise ratio. All components close to the detector wafer are made out of carefully selected materials with low intrinsic radioactivity. For further passive shielding against environmental radiation a 1.27 cm thick highly pure copper and a 3 cm thick lead shield are installed around the wafer within the warm bore of the detector magnet reducing the incident γ background by a factor of 20. A veto shield, consisting of several scintillator panels and installed around the copper and lead shielding, is used in order to tag events that are induced by cosmic muons. Furthermore, active background reduction can be achieved in the data analysis by applying a pixel-to-pixel anti-coincidence cut to removes events detected within a certain time frame, normally set to 1 µs. These so-called multi-pixel events are not

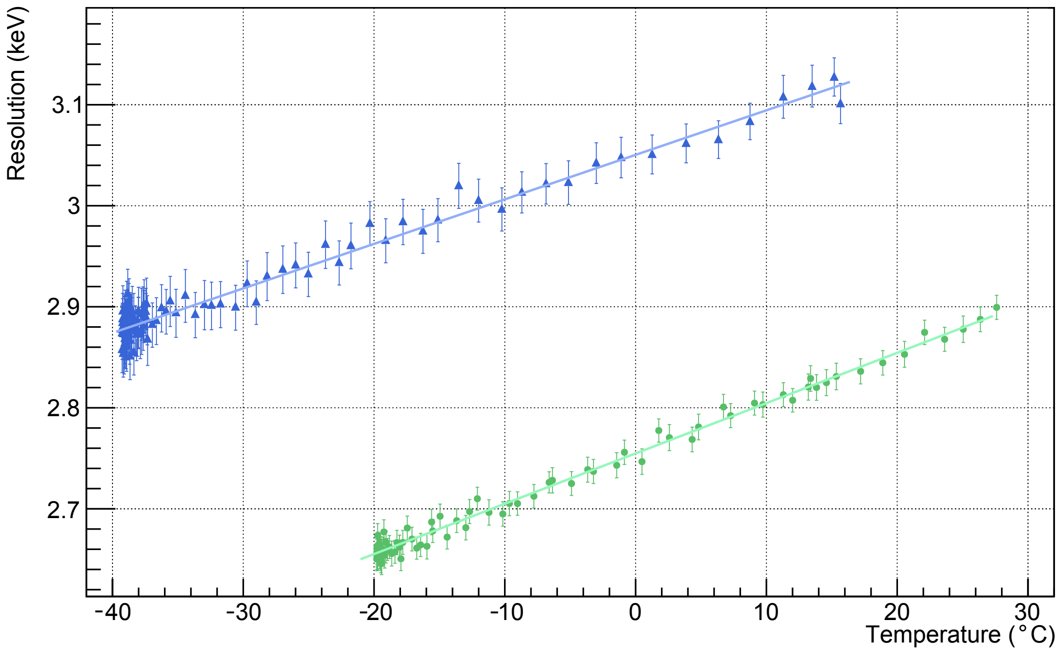

Figure 6.5: Energy resolution of SDS-IIb and test wafer as a function of the carousel temperature: The measured temperature regime shows a linear dependency of the energy resolution (FWHM), which is derived via a Gaussian fit of the 59.54 keV peak of the ^{241}Am source. The triangular points are from measurement with the test wafer with a linear fit displayed in blue, which gives a change in energy resolution of 4.4 eV/°C. Below in circular points shown is the measurement with the SDS-IIb wafer. A linear fit shown in red gives a change in energy resolution of 5.0 eV/°C.

necessarily detected on the same or adjacent pixel but can be distributed across the wafer, e.g. from cosmic rays or γs from radioactive decays passing through several pixels on the wafer. Detailed analysis concerning this cut can be found in [55, 38].

For shifting the electron energy to a region with a more favorable background level the PAE can be put on (positive) HV. Additionally, this suppresses backscattering effects since with the increasing energy the incident angle of the electrons becomes smaller and backscattering is less probable. Changing the detector a magnet field allows to optimize the diameter of the relevant magnetic flux tube on the detector and, thus, change the sensitive area on the wafer.

The measurements analyzed in this thesis were performed with the FPD system mechanically separated from the main spectrometer. This means the detector is facing the metal surface of the DN250 gate valve which occasionally emits low-energy electrons due to through passing muons. With the PAE put on (positive) voltage these low-energy electrons are accelerated towards the wafer which induces an additional background. This is observable as multiple peaks of $\mathrm{e} \cdot \mathrm{U}_{\mathrm{PAE}}$ within the detector background spectrum.

The detector background spectrum

The measured background spectrum is shown in figure 6.6. From 10 keV to lower energies a steep rise of the rate is observed which is due to the electronic noise edge below 6 keV. Between 6 and 10 keV several copper fluorescence lines induced by decays within the copper PAE appear as a region of elevated background. However, due to the limited energy resolution of the detector individual lines can not be identified. Between 10 and 120 keV the background rate is dominated by fluorescence light from surrounding materials encouraged by intrinsic radiation and cosmic rays. The rate decreases with a power law until the dominant background process changes at about 120 keV. From there on most background is induced by cosmic muons passing through the wafer. These minimal-ionizing particles induce a characteristic landau distributed background. Only a part of it is visible in the energy spectrum since at about 180 keV all events go into overflow. Overflow occurs when the events exceed an upper acceptance signal height of the DAQ. It appears as a broad peak due to baseline fluctuations of the individual channels [55, 50]. For the region of interest (ROI) for tritium β-electrons is between 15.6 keV to 20.6 keV with a background rate of 1.5 to 1.7 mcps/keV.

As the background rate at higher energies is approximately the same for the different wafers at different run times or settings, only the background rate between 0 keV and 50 keV is shown in figure 6.7 and 6.8. The data taken with the SDS-IIb wafer during SDS-IIb measurement phase is illustrated in blue, after reinstallation of this wafer is shown in red, and the data taken with the test wafer is shown in green. While no significant change of the background rate was observed after reinstallation of the SDS-IIb wafer the rate is for both measurements in general lower compared to the test wafers'. This may be due to the usage of a different feedthrough flange, the one on which the test wafer is mounted has no cylindrical donut-shaped copper sleeves for the pogo pins. These are installed in order to block internal radiation originating from the individual feedthroughs to the preamplifiers (figure 4.6). Furthermore, this increased background rate between 9 keV and 14 keV of the test wafers' data (green) may be due to an automatic threshold finder (implemented in ORCA) which sets thresholds for every pixel separately. This can lead to a shifted noise edge for

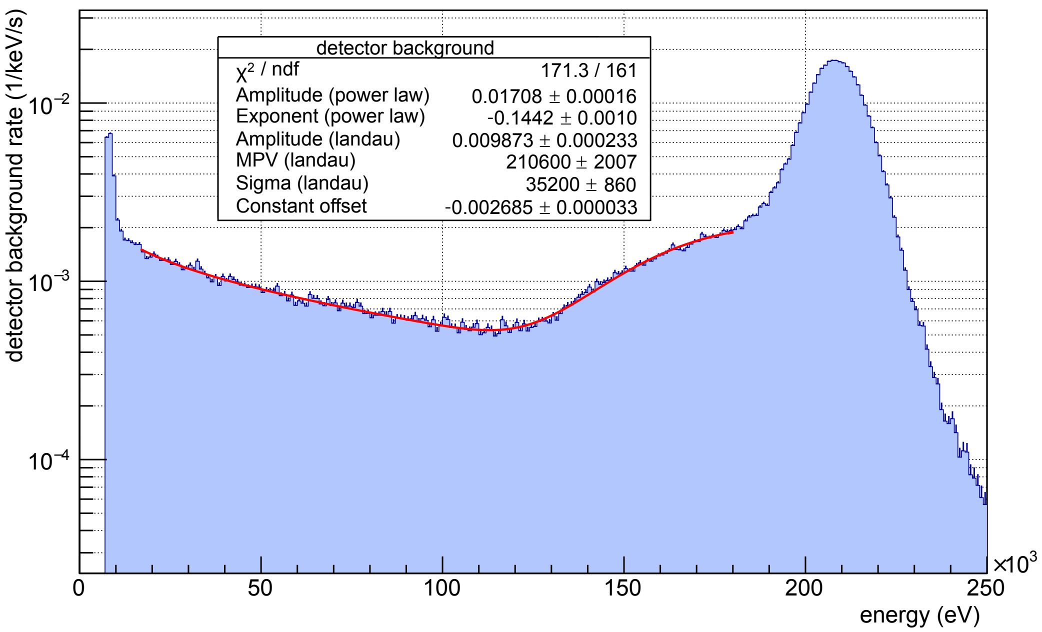

Figure 6.6: Energy spectrum of the detector background between 7 keV and 220 keV. The energy threshold at 7 keV cuts off electronic noise. At low energies fluorescence peaks originating copper PAE induce a steep rise between 7 keV and 10 keV. Up to 120 keV the background is dominated by fluorescence light originating from surrounding materials, but at higher energies the rate becomes lower. Above 120 keV the background is dominated by energy deposition within the wafer via cosmic muons which is a Landau distribution. Exceeding 180 keV the overflow peak arises with a maximum at around 200 keV. The overflow is seen as a peak due to baseline fluctuations from channel to channel.

individual pixels resulting in an increased rate in lower energy range for the mean background spectrum of the wafer, seeming like a particular background source. Comparing the background spectra of the SDS-IIb wafer (during SDS-II and after reinstallation) no significant changes are observed.

Background Measurements with the PAE on High Voltage

The PAE re-accelerates electrons which pass the MAC-E filter of the main spectrometer in order to raise their energy to an energy region with a more favorable background rate. Looking at the background spectrum in figure 6.6, a design PAE potential of $U_{PAE} = 30$ kV would shift the detector region of interest to 45.6 keV - 50.6 keV where the background level dropped to $\approx 1\,{}^{\mathrm{cps}}/_{\mathrm{keV}}$. Unfortunately, tests have that shown the PAE can only be operated stable up to 11 keV. Above this value the PAE faces the problems of breakdowns, as described in section 5.

Figure 6.8 shows the background rate between 0 keV and 50 keV for the reinstalled SDS-IIb wafer at different PAE potentials: 0 keV (red), 10 keV (green) and 10.5 keV (blue). The background rate at higher energies does not deviate from the rate measured at 0 kV. As expected, peaks at multiples of $e \cdot U_{PAE}$ are visible in the energy spectrum. The dominant peak at 10 keV (10.5 keV) is slightly shifted to a lower energy of about 9.5 keV (9.8 keV) indicating a loss of energy due to energy deposition in the dead-layer of the wafer. This effects increases for the $2 \cdot e \cdot U_{PAE}$ peaks at about 18 keV (19 keV). Peaks of higher multiplicities can not be resolved with the given

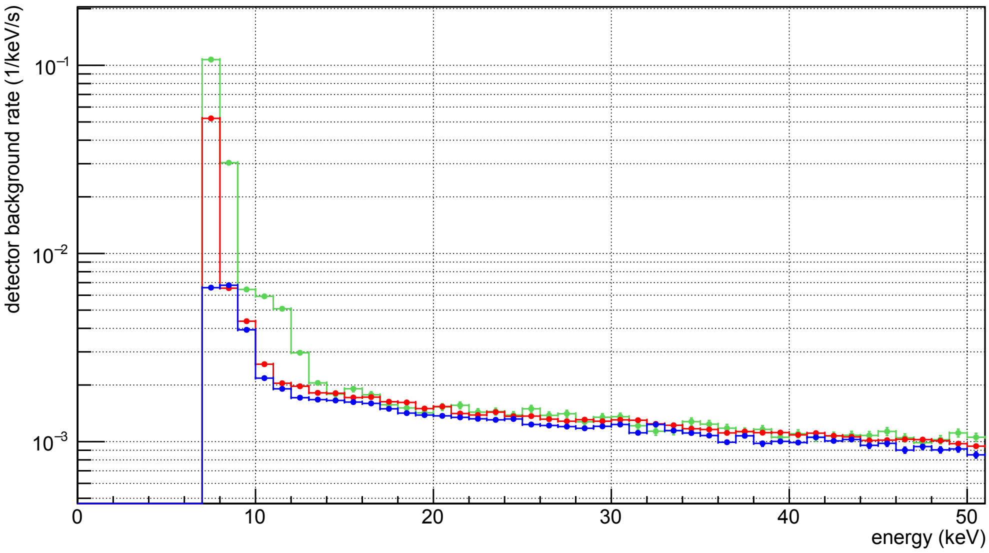

Figure 6.7: Energy spectrum of the background between 0 keV and 50 keV after applying a multi-pixel cut. Characteristic for this spectrum is the noise edge at the lower energy followed by a decreasing background rate towards higher energies. Illustrated in blue is the background rate during the SDS-IIb measurement campaign, in red after reinstalling the SDS-IIb wafer and in green the background spectrum of the test wafer. The latter shows an increased rate between 10 keV and 12 keV in comparison to the SDS-IIb wafer. The rate measured with the SDS-IIb wafer has not significantly changed.

statistics.
In the analysis the above described peaks at multiplicities of $e{\cdot}U_{PAE}$ have to be taken into account.

The measured background rate differs for different PAE potentials: In a 4 keV range around the $1{\cdot}e{\cdot}U_{PAE}$ peaks the 10.5 kV-rate is nearly twice as much as 10 kV-rate, and further the $2{\cdot}e{\cdot}U_{PAE}$ peak of 10.5 kV is still about 15% higher than the rate of the 10 kV one. This higher rate may be explained by the applied PAE voltage which induces an electric field. As described in section 5.1.1, electrons in a surface must overcome a potential barrier in order to leave the surface. An electric field deforms this barrier and, thus, increases the probability for electron tunneling which results in an increased electron rate measured at the detector wafer.

For neutrino-mass measurements the FPD system will be connected to the rest of the KATRIN beamline and, thus, additional, more dominant sources will contribute. The background sources in the spectrometer are analyzed in [38].

Besides the energy spectrum, the trend of the background rate after applying PAE potential to the FPD is of interest. When applying high voltage to the system and maintaining this state for a significant long period of time (several hours) the system is gradually conditioned resulting in a lower background rate. In figure 6.9 the background rate trend after setting the PAE to 10.5 kV (runs #28096 - #28101) is shown. The rate falls exponentially according to:

$$\mathrm{R}(t) = \mathrm{R}_0 \cdot \mathrm{e}^{-\tau \cdot t} + \mathrm{R}_1 \tag{6.1}$$

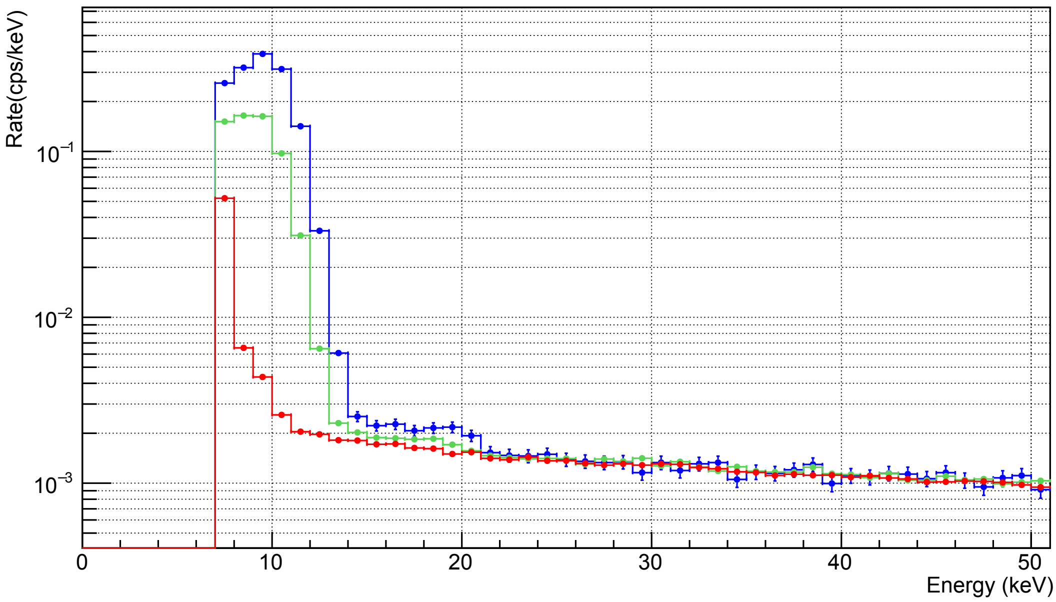

Figure 6.8: Energy spectrum of the intrinsic detector background with multi-pixel cut applied and for the reinstalled SDS-IIb wafer at different PAE voltages: In red at 0 kV, in green at +10 kV and in blue at +10.5 kV. Multiple peaks of $e{\cdot}U_{\mathrm{PAE}}$ are visible but shifted towards lower energies due to energy loss probably in the dead-layer of the detector wafer. The energy shift increases at higher multiples of $e{\cdot}U_{\mathrm{PAE}}$.

whereby R_0 is the Amplitude and R_1 represents a constant offset rate. τ is the time constant of the exponential decay. Fitting equation 6.1 to the data set at for 10.5 keV gives $R_0 = 11.91$, $R_1 = 6.57$, and $\tau_{10.5\,\mathrm{kV}} = 2.58{\cdot}10^4$ s. In comparison for runs with $U_{\mathrm{PAE}} = 10$ kV (runs #28102 - #28137) the fit gives $R_0 = 1.86$, $R_1 = 3.53$, and $\tau_{10\,\mathrm{kV}} = 1.89{\cdot}10^5$ s.

The over time decreasing background rate can be explained by a gradually conditioning of the system. This is observable as spikes during the measurements which more likely in the beginning, as shown in figures 6.10 and 6.9. These spikes originate from (micro-) discharges within the system which create free electrons when smoothening out the surfaces allowing a more stable operation of the system at HV. Another effect may appear due to charging up of an insulator (quartz tubes): Before applying HV to electrodes (PAE and foil electrodes on inside surface of quartz tubes), the system as well as the insulators are grounded. With applying HV this changes and may lead to micro-discharges between the HV electrode and the insulator resulting in a gradually charging up of the insulator due to non-conducting property. Eventually, this leads to an equilibrium.

The 10.5 kV measurement was chronological before the 10 kV measurement and can be considered as a preconditioning for the later measurement explaining the observation of a lower background rate and a higher time constant of $\tau_{10\,\mathrm{kV}} = 1.89{\cdot}10^5$ s.

This shows a conditioning of the FPD system is important in order to operate the PAE stable over a long period of time and reduce the background rate.

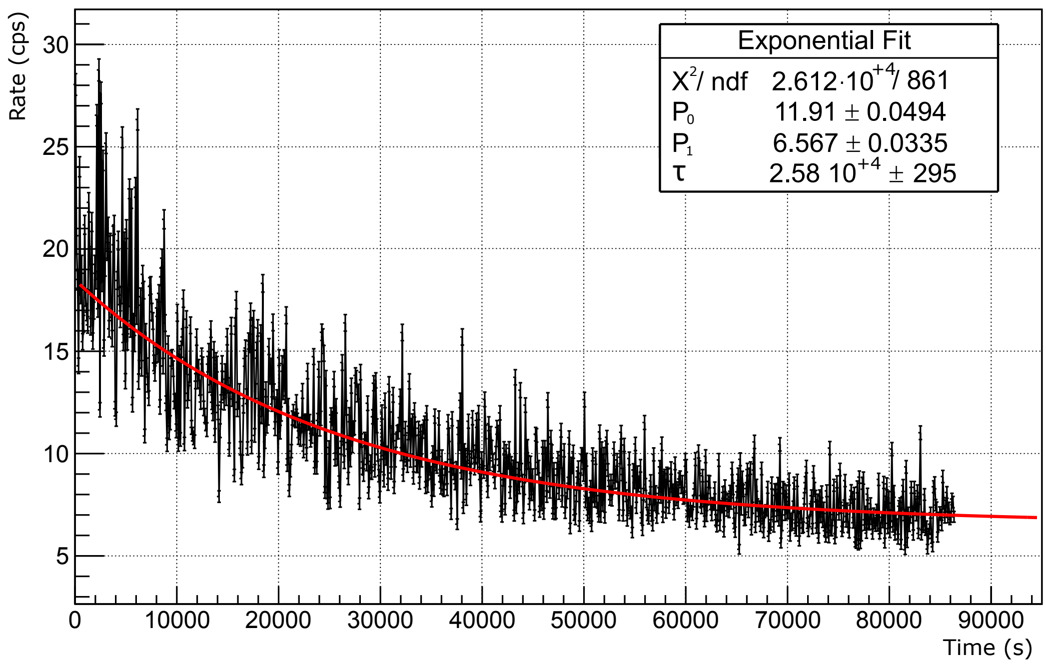

Figure 6.9: Trend of the background rate after setting the PAE to 10.5 keV. The rate drops exponentially with a time constant of $\tau = 2.58{\cdot}10^4$ s and constant factors $R_0 = 11.9$ and $R_1 = 6.57$ according to equation 6.1.

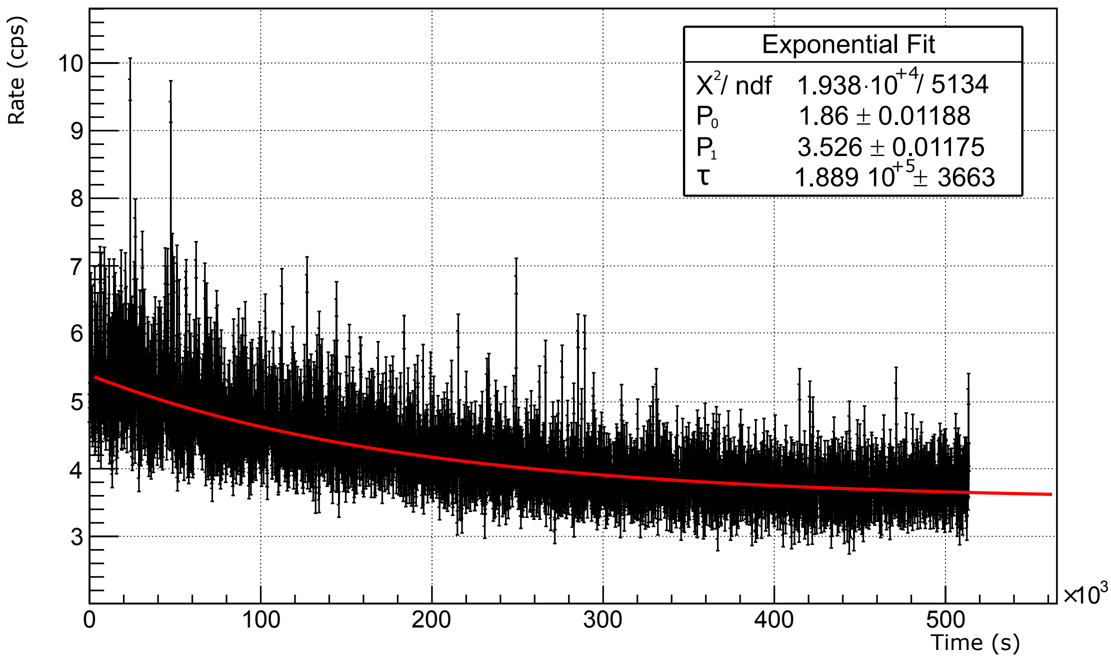

Figure 6.10: Trend of the background rate after setting the PAE to 10 keV. The rate drops exponentially with a time constant of $\tau = 1.89{\cdot}10^5$ s and constant factors $R_0 = 1.86$ and $R_1 = 3.53$ according to equation 6.1.

Table 6.1: Summary of runs taken with the SDS-IIb wafer. Calibration and background runs used for analysis are listed below. Calibration runs were taken with the ^{241}Am-source.

Runs	Comments
SDS-II measurement phase	
#20291 - #20453	Background
#20555 - #20621	Background
#23082 - #23085	Calibration
Post SDS-IIb	
#27436 - #27470	Background
#27477 - #27536	Background
#27539 - #27555	Calibration
#27556 - #27572	Background measurements
#27624 - #27712	Calibration during detector cool-down
#28096 - #28101	Background with PAE on 10.5 kV
#28102 - #28137	Background with PAE on 10 kV

Table 6.2: Summary of runs taken with the test wafer. Calibration and background runs used for analysis are listed below. Calibration runs were taken with the ^{241}Am-source

Runs	Comments
#26920 - #27031	Calibration during detector cool-down
#27134 - #27149	Calibration
#27296 - #27304	Background
#27311 - #27318	Background
#27324 - #27332	Background

7. Conclusions

The KArlsruhe TRItium Neutrino (KATRIN) experiment aims to determine the mass of the electron anti-neutrino model independently with an unsurpassed sensitivity of $m_{\bar{\nu}_e} \leq 200\,\mathrm{meV}/c^2$ (90% C.L.). To achieve this goal, the kinetic energy of electrons from tritium β-decay is measured with high precision close to the endpoint energy E_0. For this purpose KATRIN uses electrostatic retarding spectrometers based on the MAC-E filter principle which allow to scan the β-spectrum in an integral way. Since only a small fraction of all electrons will pass the analyzing plane of the experiments main-spectrometer a detector with high detection efficiency and a low intrinsic background level is needed. These requirements are fulfilled by the Focal-Plane Detector (FPD) system of KATRIN which is based on a silicon PIN-diode detector wafer. This wafer is circularly segmented in 148 pixels arranged in 12 rings (each with 12 pixels) around four Bulls-eye pixels in the center.

The objectives of this thesis were performance tests of two different wafers with regard to their spatial and energy resolution as well as their impact on the intrinsic detector background. Furthermore, a separate test stand was set up together with the KATRIN collaboration partners of the University of Washington, Seattle, in order to improve the performance of a post-acceleration electrode (PAE) which is installed inside the FPD system and is used to boost the kinetic energy of signal electrons to regimes of low intrinsic detector background.

In the first measurement campaign of the main spectrometer and detector section (SDS-I) in 2013 the used detector wafer showed a satisfying performance with a mean energy resolution of 1.5 keV, but due to two shorted pixels its spatial resolution was limited. For the subsequent measurement campaign SDS-II another detector wafer was installed into the FPD system. However, this wafer turned out to be inferior to the SDS-I one with an energy resolution 2.3 keV. Nevertheless, the SDS-II wafer was chosen to be kept installed due to the advantage of 100% functioning pixels. A third wafer (test wafer), tested in between SDS-II and the upcoming SDS-III phase, had an even worse energy resolution of about 3 keV while still providing 100% functioning pixels. After reinstalling the SDS-II wafer a degradation of its energy resolution to 2.6 keV was discovered. In order to exclude the readout and amplification devices of the detector as cause of the observed degradation a series of test measurements were carried out. These showed no influence of the electronics on the energy resolution, leaving the wafer itself as remaining candidate for the performance loss over time. The cause of this degradation trend is yet still unknown. However, the variety of energy resolutions for the different wafers can be explained by different qualities of different batches of wafers.
Via an analysis of the single-pixel energy resolutions the spatial resolution of the

different detector wafers was investigated. For all four wafers tested in the past few years, a tendency showing an improvement of the single-pixel energy resolutions towards inner pixel rings is observed. This may have several explanations: Firstly, the bias ring, used for biasing the detector wafer from its backside, may have an influence on the outer pixel rings despite a 2 mm thick guard ring. Secondly, it is to be mentioned that the pressure on the detector wafer induced by the signal feedthrough pins might influence the individual pixels, but previous investigations could exclude this explanation for the most part. As it is a semiconductor, the performance of the detector wafer is highly temperature dependent. Measurements taken in a temperature range of -38°C to +28°C showed a linear relation between the mean energy resolution and the temperature. However, for lower temperatures the energy resolution reaches a constant plateau and for higher temperatures it degrades exponentially. This is explainable by thermal noise as well as leakage current becoming more dominant at higher temperatures.

Besides the energy resolution one key parameter characterizing the detector performance is the intrinsic detector background spectrum. Comparing the background spectra of the test wafer and SDS-II wafer show similar background rates above 30 keV. In the lower energy range close to the noise edge, however, the measured background rates differ. This is most likely due to per-channel thresholds which are automatically determined by the data acquisition (DAQ) software. Furthermore, a contribution to the background can also originate from the different feedthrough flanges used. In difference to the test wafer the flange on which the SDS-II wafer was mounted had copper sleeves around each signal feedthrough pin installed. These sleeves are used to shield the wafer from radiation originating from the feedthrough flange. Regarding the region of interest for tritium measurements (15.6 keV to 30.6 keV) the background rate is between $1.5 - 1.7\ ^{\mathrm{mcps}}/_{\mathrm{keV}}$.
Applying high voltage to the PAE allows to shift the region of interest (ROI) to an energy range with a more favorable background rate. By applying a voltage of 10 kV (10.5 kV) the ROI is shifted to 25.6 keV $-$ 30.6 keV (26.1 keV $-$ 21.1 keV) which an average background rate of $1\ ^{\mathrm{mcps}}/_{\mathrm{keV}}$ improving the signal-to-noise ratio.
The background rate trend measured directly after applying high voltage shows a gradual reduction over a long period of time (several hours). This behavior may be explained by a gradually conditioning of the system, a hypothesis further supported by the observation of small spikes in the rate trend which appear less frequent with increasing measurement time. These spikes can be attributed to (micro-) discharges within the system temporarily increasing the measured background rate. Such discharges smoothen out the surfaces which allows a more stable operation of the system at high voltage.

To this point it is not possible to operate the PAE at voltages higher than 11 kV. A separate test stand was build which is located at the University of Washington, Seattle, to test the PAE without risking damage to the sensitive electronics used in the real system. The test stand uses vacuum chamber without the readout electronics, custom made parts (observation window and blanking flange) and has no magnetic field. The latter is possible because the occurrence of breakdowns is independent from magnetic fields. A custom made blanking flange turned out not to be vacuum suitable which limits the achievable vacuum pressure to the 10^{-3} mbar regime. Vacuum test were carried out to visually observe discharge processes within the PAE chamber for the first time. The observations confirmed the results of previously carried out simulation indicating regions of high electric field inside the PAE chamber. However, more tests at lower vacuum pressure, preferably in the same regime as at the FPD (10^{-6} mbar), are necessary for a better understanding of the breakdown phenomena. The test stand as a starting point for further developments may lead a more effective method to condition the FPD system without harming sensitive read-out electronics.

Bibliography

[1] J. Chadwick, “Intensitätsverteilung im magnetischen spektrum der β-strahlen von radium b+c,” *Verhanlungenden Deutschen Physikalischen Gesellschaft*, vol. 16, no. 1, pp. 383 – 391, 1914.

[2] W. Pauli, R. Kronig, and V. Weisskopf, *Collected scientific papers.* New York, NY: Interscience, 1964, offener Brief an die Gruppe der Radioaktiven bei der Gauvereinstagung zu Tübingen (datiert 4. Dez. 1930).

[3] J. Chadwick, “The existence of a neutron,” in *Proceedings of the Royal Society of London A: Mathematical, Physical and Engineering Sciences*, vol. 136, no. 830. The Royal Society, 1932, pp. 692–708.

[4] E. Fermi, “Versuch einer theorie der β-Strahlen.” *Zeitschrift für Physik*, vol. 88, no. 3–4, pp. 161–177, 1934.

[5] H. Bethe and R. Peierls, “The’neutrino’,” *Nature*, vol. 133, no. 3362, p. 532, 1934.

[6] F. Reines and C. L. Cowan, “The neutrino,” *Nature*, vol. 178, no. 4531, pp. 446–449, 1956.

[7] G. Danby et al., “Observation of high-energy neutrino reactions and the existence of two kinds of neutrinos,” *Physical Review Letters*, vol. 9, no. 1, p. 36, 1962.

[8] M. L. Perl et al., “Evidence for anomalous lepton production in e+- e- annihilation,” *Physical Review Letters*, vol. 35, no. 22, p. 1489, 1975.

[9] P. W. Higgs, “Broken symmetries and the masses of gauge bosons,” *Physical Review Letters*, vol. 13, no. 16, p. 508, 1964.

[10] C. ALEPH, DELPHI, L3, OPAL, SLD, L. E. W. Group *et al.*, “Precision electroweak measurements on the z resonance,” *arXiv preprint hep-ex/0509008*, 2005.

[11] B. Pontecorvo, “Inverse *beta* processes and nonconservation of lepton charge,” *Zhur. Eksptl'. i Teoret. Fiz.*, vol. 34, 1958.

[12] J. N. Bahcall, “Solar neutrino cross sections and nuclear beta decay,” *Phys. Rev.*, vol. 135, pp. B137–B146, Jul 1964. [Online]. Available: http://link.aps.org/doi/10.1103/PhysRev.135.B137

[13] R. Davis Jr, D. S. Harmer, and K. C. Hoffman, “Search for neutrinos from the sun,” *Physical Review Letters*, vol. 20, no. 21, p. 1205, 1968.

[14] J. N. Bahcall and R. Davis, “Solar Neutrinos - a Scientific Puzzle,” *Science*, vol. 191, pp. 264–267, 1976.

[15] W. Hampel, J. Handt, G. Heusser *et al.*, "GALLEX solar neutrino observations: results for GALLEX IV," *Physics Letters B*, vol. 447, no. 1–2, pp. 127 – 133, 1999. [Online]. Available: http://www.sciencedirect.com/science/article/pii/S0370269398015792

[16] M. Altmann, M. Balata, P. Belli *et al.*, "Complete results for five years of GNO solar neutrino observations," *Physics Letters B*, vol. 616, no. 3–4, pp. 174 – 190, 2005. [Online]. Available: http://www.sciencedirect.com/science/article/pii/S0370269305005149

[17] J. N. Bahcall, "Solar neutrinos. i. theoretical," *Phys. Rev. Lett.*, vol. 12, pp. 300–302, Mar 1964. [Online]. Available: http://link.aps.org/doi/10.1103/PhysRevLett.12.300

[18] B. Pontecorvo, "Neutrino Experiments and the Problem of Conservation of Leptonic Charge," *Sov. Phys. JETP*, vol. 26, pp. 984–988, 1968, [Zh. Eksp. Teor. Fiz.53,1717(1967)].

[19] R. Helmer, "First results from the sudbury neutrino observatory," *Nuclear Physics B - Proceedings Supplements*, vol. 111, no. 1, pp. 122 – 127, 2002. [Online]. Available: http://www.sciencedirect.com/science/article/pii/S0920563202016936

[20] A. Bellerive, J. Klein, A. McDonald, A. Noble, and A. Poon, "The sudbury neutrino observatory," *Nuclear Physics B*, vol. 908, pp. 30 – 51, 2016, neutrino Oscillations: Celebrating the Nobel Prize in Physics 2015. [Online]. Available: http://www.sciencedirect.com/science/article/pii/S0550321316300736

[21] B. Pontecorvo, "Inverse beta processes and nonconservation of lepton charge," *Sov. Phys. JETP*, vol. 7, pp. 172–173, 1958, [Zh. Eksp. Teor. Fiz.34,247(1957)].

[22] Z. Maki, M. Nakagawa, and S. Sakata, "Remarks on the Unified Model of Elementary Particles," *Progress of Theoretical Physics*, vol. 28, pp. 870–880, Nov. 1962.

[23] S. P. Mikheev and A. Yu. Smirnov, "Resonant amplification of neutrino oscillations in matter and solar neutrino spectroscopy," *Nuovo Cim.*, vol. C9, pp. 17–26, 1986.

[24] Y. Fukuda *et al.*, "The Super-Kamiokande detector," *Nucl. Instrum. Meth.*, vol. A501, pp. 418–462, 2003.

[25] T. Gaisser and F. Halzen, "Icecube," *Annual Review of Nuclear and Particle Science*, vol. 64, no. 1, pp. 101–123, 2014. [Online]. Available: http://dx.doi.org/10.1146/annurev-nucl-102313-025321

[26] S. F. King and C. Luhn, "Neutrino Mass and Mixing with Discrete Symmetry," *Rept. Prog. Phys.*, vol. 76, p. 056201, 2013.

[27] J. Lesgourgues and S. Pastor, "Neutrino cosmology and Planck," *New J. Phys.*, vol. 16, p. 065002, 2014.

[28] M. Agostini *et al.*, "Results on Neutrinoless Double-β Decay of ^{76}Ge from Phase I of the GERDA Experiment," *Phys. Rev. Lett.*, vol. 111, no. 12, p. 122503, 2013.

[29] D. G. Phillips, II *et al.*, "The Majorana experiment: an ultra-low background search for neutrinoless double-beta decay," *J. Phys. Conf. Ser.*, vol. 381, p. 012044, 2012.

[30] M. Schlösser, "Accurate calibration of the raman system for the karlsruhe tritium neutrino experiment," Ph.D. dissertation, Karlsruher Institut für Technologie (KIT), 2013.

[31] S. R. Elliott and P. Vogel, "Double beta decay," *Annual Review of Nuclear and Particle Science*, vol. 52, no. 1, pp. 115–151, 2002. [Online]. Available: http://dx.doi.org/10.1146/annurev.nucl.52.050102.090641

[32] P. A. M. Dirac, "The quantum theory of the emission and absorption of radiation," *Proceedings of the Royal Society of London A: Mathematical, Physical and Engineering Sciences*, vol. 114, no. 767, pp. 243–265, 1927. [Online]. Available: http://rspa.royalsocietypublishing.org/content/114/767/243

[33] H. Barth, A. Bleile, J. Bonn *et al.*, "The status of the mainz neutrino mass experiment," *Nuclear Physics B - Proceedings Supplements*, vol. 66, no. 1, pp. 183 – 186, 1998. [Online]. Available: http://www.sciencedirect.com/science/article/pii/S0920563298000310

[34] V. N. Aseev, A. I. Belesev, A. I. Berlev *et al.*, "Measurement of the electron antineutrino mass in tritium beta decay in the Troitsk nu-mass experiment," *Physics of Atomic Nuclei*, vol. 75, no. 4, pp. 464–478, 2012. [Online]. Available: http://dx.doi.org/10.1134/S1063778812030027

[35] K. Olive and P. D. Group, "Review of particle physics," *Chinese Physics C*, vol. 38, no. 9, p. 090001, 2014. [Online]. Available: http://stacks.iop.org/1674-1137/38/i=9/a=090001

[36] KATRIN collaboration, "KATRIN design report," *FZKA scientific report*, vol. 7090, 2005. [Online]. Available: http://bibliothek.fzk.de/zb/berichte/FZKA7090.pdf

[37] J. Wolf, "The {KATRIN} neutrino mass experiment," *Nuclear Instruments and Methods in Physics Research Section A: Accelerators, Spectrometers, Detectors and Associated Equipment*, vol. 623, no. 1, pp. 442 – 444, 2010, 1st International Conference on Technology and Instrumentation in Particle Physics. [Online]. Available: http://www.sciencedirect.com/science/article/pii/S0168900210005942

[38] A. Müller, "Investigation of the secondary electron emission characteristics of the KATRIN main spectrometer," Master Thesis, Karlsruher Institut für Technologie (KIT), 2015. [Online]. Available: https://fuzzy.fzk.de/bscw/bscw.cgi/1043002?op=preview&back_url=15294%3fclient_size%3d1920x889

[39] N. Wandkowsky, "Study of background and transmission properties of the KATRIN spectrometers," Ph.D. dissertation, Karlsruher Institut für Technologie (KIT), 2013. [Online]. Available: http://digbib.ubka.uni-karlsruhe.de/volltexte/1000036631

[40] S. Groh, "Modeling of the response function and measurement of transmission properties of the KATRIN experiment," Ph.D. dissertation,

Karlsruher Institut für Technologie (KIT), 2015. [Online]. Available: http://nbn-resolving.org/urn:nbn:de:swb:90-465464

[41] S. Grohmann, T. Bode, H. Schön, and M. Süßer, "Precise temperature measurement at 30 k in the KATRIN source cryostat," *Cryogenics*, vol. 51, no. 8, pp. 438–445, 2011.

[42] T. B. Windberger, "Optimierung des 2-phasen-kühlkonzepts für den wgts-demonstrator von KATRIN," Diploma Thesis, Karlsruher Institut für Technologie (KIT), 2011.

[43] S. Grohmann, T. Bode, M. Hötzel, H. Schön, M. Süßer, and T. Wahl, "The thermal behaviour of the tritium source in KATRIN," *Cryogenics*, vol. 55-56, no. 0, pp. 5–11, 2013.

[44] M. Schlösser, S. Fischer, M. Sturm, B. Bornschein, R. Lewis, and H. Telle, "Design implications for laser raman measurement systems for tritium sample-analysis, accountancy or process-control applications," *Fusion Science and Technology*, vol. 60, no. 3, pp. 976–981, 2011. [Online]. Available: http://www.ans.org/pubs/journals/fst/a_12579

[45] M. Sturm, "Bestimmung der tritiumflussreduktion einer tritium-argon-frostpumpe für das neutrinomassenexperiment KATRIN," Diploma Thesis, Universität Karlsruhe (TH), 2007. [Online]. Available: http://www.katrin.kit.edu/publikationen/dth-sturm.pdf

[46] M. Ubieto Díaz, "Off-line commissioning of a non-destructive FT-ICR detection system for monitoring the ion concentration in the KATRIN beamline," Ph.D. dissertation, Ruperto-Carola University of Heidelberg, 2011. [Online]. Available: http://pubman.mpdl.mpg.de/pubman/item/escidoc:1255588:2/component/escidoc:1255587/2Ubieto_Thesis.pdf

[47] M. Ubieto-Díaz, D. Rodríguez, S. Lukic, S. Nagy, S. Stahl, and K. Blaum, "A broad-band FT-ICR penning trap system for KATRIN," *International Journal of Mass Spectrometry*, vol. 288, no. 1–3, pp. 1–5, 2009.

[48] M. Hackenjos, "Die differentielle pumpstrecke des KATRIN-experiments - inbetriebnahme und charakterisierung des supraleitenden magnetsystems," Master Thesis, Karlsruher Institut für Technologie (KIT), 2015. [Online]. Available: http://www.katrin.kit.edu/publikationen/MaT_Hackenjos.pdf

[49] A. Windberger, "Berechnungen und simulationen zum verhalten von ionen in der differenziellen pumpstrecke des KATRIN-experiments," Diploma Thesis, Karlsruher Institut für Technologie (KIT), 2011. [Online]. Available: http://www.katrin.kit.edu/publikationen/dth-windberger.pdf

[50] F. Harms, "Characterization and minimization of background processes in the katrin main spectrometer," Ph.D. dissertation, Karlsruher Institut für Technologie (KIT), 2015. [Online]. Available: http://nbn-resolving.org/urn:nbn:de:swb:90-500274

[51] W. Gil, J. Bonn, B. Bornschein, R. Gehring, O. Kazachenko, J. Kleinfeller, and S. Putselyk, "The Cryogenic Pumping Section of the KATRIN experiment," *IEEE Transactions on Applied Superconductivity*, vol. 20, no. 3, pp. 316–319, 2010.

[52] R. Bottesch, "Set-up of the motion control and characterization of the ablation laser for the condensed ^{83m}Kr conversion electron source of the KATRIN experiment," Diploma Thesis, Westfälische Wilhelms-Universität Münster, 2012. [Online]. Available: http://www.uni-muenster.de/Physik.KP/AGWeinheimer/Files/theses/Diplom_Richard_Bottesch.pdf

[53] M. Prall, P. Renschler, F. Glück, A. Beglarian, H. Bichsel, L. Bornschein, Z. Chaoui, G. Drexlin, F. Fränkle, S. Görhardt, S. Mertens, M. Steidl, T. Thümmler, S. Wüstling, C. Weinheimer, and S. Zadorozhny, "The KATRIN pre-spectrometer at reduced filter energy," *New Journal of Physics*, vol. 14, no. 7, p. 073054, 2012.

[54] F. Glück, G. Drexlin, B. Leiber, S. Mertens, A. Osipowicz, J. Reich, and N. Wandkowsky, "Electromagnetic design of the large-volume air coil system of the KATRIN experiment," *New Journal of Physics*, vol. 15, no. 8, p. 083025, 2013.

[55] J. S. Schwarz, "The detector system of the KATRIN experiment - implementation and first measurements with the spectrometer," Ph.D. dissertation, Karlsruher Institut für Technologie (KIT), 2014. [Online]. Available: http://nbn-resolving.org/urn:nbn:de:swb:90-427724

[56] B. Leiber, "Investigations of background due to secondary electron emission in the KATRIN-experiment," Ph.D. dissertation, Karlsruher Institut für Technologie (KIT), 2014. [Online]. Available: http://nbn-resolving.org/urn:nbn:de:swb:90-424154

[57] J. Barrett, A. Beglarian, J. Behrens *et al.*, "Results of the first KATRIN SDS measurement phase," *internal KATRIN document*, 2014.

[58] F. R. Müller, "Efficiency studies of the background suppression by a liquid-nitrogen cooled baffle system in the katrin experiment," Master Thesis, Karlsruher Institut für Technologie (KIT), 2015. [Online]. Available: https://fuzzy.fzk.de/bscw/bscw.cgi/966078?op=preview&back_url=15294%3fclient_size%3d1920x889

[59] F. Bandenburg, "Inbetriebnahme des fokalebenendetektor-systems für eine zweite messphase am KATRIN-hauptspektrometer," Diploma Thesis, Karlsruher Institut für Technologie (KIT), 2014.

[60] E. L. Martin, "FPD wafer test board," *internal KATRIN document*, 2014. [Online]. Available: https://fuzzy.fzk.de/bscw/bscw.cgi/875187?op=preview&back_url=1005301

[61] S. Schmid, "Performance des fokalebenendetektors zu beginn der zweiten gemeinsamen messphase mit dem KATRIN hauptspektrometer," Bachelor Thesis, Karlsruher Institut für Technologie (KIT), 2014.

[62] J. Amsbaugh, J. Barrett, A. Beglarian *et al.*, "Focal-plane detector system for the KATRIN experiment," *Nuclear Instruments and Methods in Physics Research Section A: Accelerators, Spectrometers, Detectors and Associated Equipment*, vol. 778, pp. 40–60, 2015.

[63] F. Harms, "Assembly and first results of the KATRIN focal-plane detector system at KIT," Diploma Thesis, Karlsruher Institut für Technologie (KIT),

2012. [Online]. Available: http://www.katrin.kit.edu/publikationen/dth_Fabian_Harms.pdf

[64] J. F. Amsbaugh, N. M. Boyd, and D. M. S. Parno, “Runge-kutta method for numerical solution of differential equation system,” *internal KATRIN document*, 2012. [Online]. Available: https://fuzzy.fzk.de/bscw/bscw.cgi/1012705?op=preview&back_url=1005301

[65] C. Kittel, *Einführung in die Festkörperphysik*, 15th ed. München: Oldenbourg, 2013. [Online]. Available: http://deposit.d-nb.de/cgi-bin/dokserv?id=4223635&prov=M&dok_var=1&dok_ext=htm;http://d-nb.info/1029368872/04

[66] B. VanDevender, L. Bodine, A. Myers *et al.*, “Performance of a TiN-coated monolithic silicon pin-diode array under mechanical stress,” *Nuclear Instruments and Methods in Physics Research Section A: Accelerators, Spectrometers, Detectors and Associated Equipment*, vol. 673, no. 0, pp. 46–50, 2012.

[67] G. F. Knoll, *Radiation detection and measurement; 4th ed.* New York, NY: Wiley, 2010. [Online]. Available: https://cds.cern.ch/record/1300754

[68] Johannes and Sascha, “Feedthrough flange and wafer #96728 inspection,” 2012. [Online]. Available: https://crunch5.npl.washington.edu:8443/KATRIN+Detector+Commissioning+/485

[69] F. Fränkle, “Visual inspection of wafer #115877,” 2016, main-detector, Message ID: 13. [Online]. Available: https://neutrino.ikp.kit.edu:8080/main-detector/13

[70] A. Seher, “Visual inspection of wafer #115875,” 2016, main-detector, Message ID: 16. [Online]. Available: https://neutrino.ikp.kit.edu:8080/main-detector/16

[71] V. T. Jordanov and G. F. Knoll, “Digital synthesis of pulse shapes in real time for high resolution radiation spectroscopy,” *Nuclear Instruments and Methods in Physics Research Section A: Accelerators, Spectrometers, Detectors and Associated Equipment*, vol. 345, no. 2, pp. 337 – 345, 1994. [Online]. Available: http://www.sciencedirect.com/science/article/pii/0168900294910111

[72] J. Formaggio, “The KATRIN veto and shield system,” *internal KATRIN document*, 2007.

[73] J. D. Craggs and J. M. J. M. Meek, *Electrical breakdown of gases*, rev. ed ed. Chichester ; New York : Wiley, 1978, "A Wiley-Interscience publication.".

[74] V. A. Nevrovsky, V. I. Rakhovsky, and V. G. Zhurbenko, “Dc breakdown of ultra-high vacuum gaps,” *Beiträge aus der Plasmaphysik*, vol. 23, no. 4, pp. 433–458, 1983. [Online]. Available: http://dx.doi.org/10.1002/ctpp.19830230410

[75] “Front matter,” in *Physical Methods in Chemical Analysis*, W. G. BERL, Ed. Academic Press, 1956, pp. iii –. [Online]. Available: http://www.sciencedirect.com/science/article/pii/B9781483232386500019

[76] F. Glück, “The penning discharge,” *internal KATRIN document*, 2007. [Online]. Available: https://fuzzy.fzk.de/bscw/bscw.cgi/354775?op=preview&back_url=354761%3fclient_size%3d1920x920

[77] F. Paschen, "Ueber die zum funkenübergang in luft, wasserstoff und kohlensäure bei verschiedenen drucken erforderliche potentialdifferenz," *Annalen der Physik*, vol. 273, no. 5, pp. 69–96, 1889. [Online]. Available: http://dx.doi.org/10.1002/andp.18892730505

[78] W. contributors, "Sensitivity of next-generation tritium beta-decay experiments for kev-scale sterile neutrinos," *Wikipedia, The Free Encyclopedia.* [Online]. Available: https://en.wikipedia.org/w/index.php?title=Microplasma&oldid=686991284

[79] F. M. Fränkle, "Background investigations of the KATRIN pre-spectrometer," Ph.D. dissertation, Karlsruher Institut für Technologie (KIT), 2010. [Online]. Available: http://nbn-resolving.org/urn:nbn:de:swb:90-193929

[80] S. Groh, "Untersuchung von uv-laser induziertem untergrund am KATRIN vorspektrometer," Diploma Thesis, Karlsruher Institut für Technologie (KIT), 2010. [Online]. Available: http://www.katrin.kit.edu/publikationen/dth-groh.pdf

[81] A. Picard, H. Backe, H. Barth *et al.*, "A solenoid retarding spectrometer with high resolution and transmission for kev electrons," *Nuclear Instruments and Methods in Physics Research Section B: Beam Interactions with Materials and Atoms*, vol. 63, no. 3, pp. 345–358, 1992.

[82] F. Penning, "Die glimmentladung bei niedrigem druck zwischen koaxialen zylindern in einem axialen magnetfeld," *Physica*, vol. 3, no. 9, pp. 873 – 894, 1936. [Online]. Available: http://www.sciencedirect.com/science/article/pii/S0031891436803139

[83] F. Fränkle, F. Glück, K. Valerius *et al.*, "Penning discharge in the KATRIN pre-spectrometer," *Journal of Instrumentation*, vol. 9, no. 7, p. P07028, 2014.

[84] A. Müller, "High voltage simulation of the PAE," *internal KATRIN document*, 2014.

Acknowledgments

Abschließend möchte ich mich an dieser Stelle ganz herzlich bei allen bedanken, die mich im letzten Jahr begleitet, unterstützt und zum Gelingen meiner Masterarbeit beigetragen haben. Ein besonderer Dank gilt hierbei im Besonderen:

- Prof. Dr. Guido Drexlin für die Möglichkeit meine Masterabeit bei KATRIN schreiben zu dürfen.
- Prof. Wim de Boer dafür, dass er freundlicherweise das Korreferat übernommen hat.
- Dr. Fabian Harms für die ausgezeichnete fachliche und persönliche Betreuung, sowie die vielen hilfreichen Tipps und Anregungen zu dieser Arbeit.
- Dr. Florian Fränkle für die zahlreichen und interessanten Diskussionen, die großartige Zusammenarbeit im Büro sowie am FPD System.
- Thank you Prof. Peter Doe and Prof. Diana Parno for giving me the opportunity to stay at CENPA for several weeks and all other colleges from the US collaboration partners, for their support and help during the assembly of the PAE test stand.
- Dr. Bianca Keilhauer, stellvertretend für das i-Progress Programm, für die finanzielle Unterstützung während meines Aufenthalts in den USA.
- Allen Technikern, Doktoranden, Postdocs und weiteren beteiligten Personen, die uns bei der Wiederinbetriebnahme des FPD Systems unterstützt haben.
- Allen, die in diesem Jahr Kuchen mitgebracht, Pizza bestellt sowie geholt und die Mittags- und Kaffeepausen bereichert haben.

Besonderen Dank gilt meinen Eltern und meinen Geschwistern, die mich während des Studiums immer unterstützt haben und Rückhalt gegeben haben. Im besonderen möchte ich meinem Vater, Dieter H. E. Seher, danken, der mich bereits in früher Kindheit den Naturwissenschaften nahe gebracht und zu diesem Studium ermutigt hat, jedoch meinen Abschluss an dieser Stelle nicht mehr mit erleben durfte.